Physics of Fluids ARTICLE pubs.aip.org/aip/pof

Nonlinear hydroelastic responses of a submerged horizontal plate under focused wave conditions: A cumulative fatigue perspective

Cite as: Phys. Fluids **37**, 017110 (2025); doi: 10.1063/5.0246534
Submitted: 2 November 2024 · Accepted: 11 December 2024 ·
Published Online: 6 January 2025

View Online Export Citation CrossMark

Haoyu Ding,[1] Luofeng Huang,[2] and Jun Zang[1,a)]

AFFILIATIONS

[1]Department of Architecture & Civil Engineering, University of Bath, Bath BA2 7AY, England, United Kingdom
[2]Faculty of Engineering and Applied Sciences, Cranfield University, Cranfield MK43 0AL, England, United Kingdom

Note: This paper is part of the Special Topic, Wave-Structure Interaction.
[a)]**Author to whom correspondence should be addressed:** j.zang@bath.ac.uk

ABSTRACT

Most current analytical research on the hydroelastic interaction between water waves and submerged horizontal elastic plates remains within the scope of linear theory due to the underdevelopment of mathematical methods for solving nonlinear problems. To address this gap, this work employs an approach that combines computational fluid dynamics (CFD) with computational solid mechanics (CSM) to dynamically simulate the fully coupled nonlinear hydroelastic interactions between ocean waves and a submerged horizontal plate. This research highlights the significance of nonlinear point responses of a submerged horizontal plate under focused wave conditions. A phase-based harmonic separation method (i.e., phase-decomposition method) is used to isolate wave amplitude and force harmonic components in complex wave scenarios. This approach allows for the clean delineation of individual harmonics from the total wave force by controlling the phase of incident focused waves and is for the first time applied to the response analysis of elastic structures. This paper successfully used the phase-decomposition method to separate the individual harmonics of the point displacement of a horizontal elastic plate, directly demonstrating the significance of nonlinear responses. Additionally, the impact of plate rigidity, which relates to natural frequency, on nonlinear responses is investigated. The results indicate that plates with a certain dimensionless plate rigidity will exhibit more significant nonlinear responses. By cleanly separating each individual harmonic response, this study provides new insights into the nonlinear hydroelastic responses of a horizontal plate interacting with water waves and offers a new perspective on fatigue analysis, underscoring the importance of nonlinearity for future engineering designs.

© 2025 Author(s). All article content, except where otherwise noted, is licensed under a Creative Commons Attribution (CC BY) license (https://creativecommons.org/licenses/by/4.0/). https://doi.org/10.1063/5.0246534

06 January 2025 12:39:23

I. INTRODUCTION

In recent decades, intensive research has been conducted on the hydroelastic interaction between water waves and elastic plates in ocean and polar engineering, driven by both academic interest and practical applications. Elastic plates, which are envisioned to serve in applications such as floating airports, artificial islands, breakwaters, wave energy converters, and other offshore infrastructure, are often modeled as flexible structures interacting with fluid environments. These plates are characterized by their significant flexibility and large horizontal scales relative to their vertical dimensions and characteristic wavelengths. Consequently, understanding hydroelastic deformation in response to water waves is crucial for the safe and economical design and maintenance of such offshore elastic structures. Early studies in this field mainly focused on the hydroelastic interaction between water waves and large ice sheets, which were idealized as elastic plates.[1] These elastic plates were often assumed to be semi-infinitely long compared to the wavelength of the incident wave.[2,3] Comprehensive summaries of early work can be found in several review papers.[3–5] However, due to the underdevelopment of mathematical methods for solving nonlinear problems, most current analytical research on the hydroelastic interaction between water waves and elastic plates remains within the scope of linear theory.

This paper specifically investigates a submerged horizontal plate. Early studies on submerged horizontal plates were mostly analytical. Heins[6] is considered one of the pioneers in studying a semi-infinite width plate interacting with waves in a finite water depth. Green and

© Author(s) 2025

Heins[7] extended the analytical solution to infinite water depth. Burke[8] further developed a mathematical method for a submerged finite-width plate based on the Wiener–Hopf method. Alternative analytical methods such as matched asymptotic expansions in Refs. 9 and 10 and the eigenfunction expansion method in Refs. 11–13 have also been applied to relevant problems. Hassan *et al.*[14] used the eigenfunction expansion method to examine wave interaction with submerged elastic plates, focusing on wave reflection, transmission, and the effects of plate elasticity and submergence depth on wave behavior in both deep and shallow waters. Mohapatra and Sahoo[15] employed the eigenfunction expansion method to model the linear wave interaction with floating and submerged elastic plate systems, assuming small amplitude surface waves and structural responses. Porter[16] developed a semi-analytical model using the eigenfunction expansion method to study linear wave interaction with submerged horizontal plates, emphasizing wave transmission, reflection, and wave-induced forces in both finite and infinite water depths.

In recent years, the fully nonlinear computational fluid dynamics (CFD) method has been extensively used to investigate wave interactions with submerged horizontal plates. Qi and Hou[17] modeled the transmission of nonlinear waves over a submerged horizontal plate using CFD, demonstrating the method's capability to simulate nonlinear wave behavior over the plate. Jin *et al.*[18] applied a two-phase CFD solver to investigate the performance of a rigid and fixed submerged horizontal plate in waves, finding that a relatively thin plate has better wave damping performance than a thick one. He *et al.*[19,20] used a CFD approach based on the smoothed particle hydrodynamics method (a Lagrangian-based mesh-free method) to study the effect of non-breaking and breaking waves on a fixed submerged horizontal plate. He *et al.*[21] and Fu *et al.*[22] performed numerical simulations of waves interacting with a heaving submerged horizontal plate, finding that a heaving plate can be more effective than a fixed one in most submerged conditions. Yueh *et al.*[23] proposed a concept of a submerged wavy plate breakwater, which showed better wave attenuating performance in certain situations with proper design, although practical considerations such as manufacturing cost and structural strength need further investigation.

Despite the capability of CFD to model nonlinear wave effects and simulate flows with minimal assumptions, previous studies typically assumed long thin submerged horizontal plates as rigid bodies because CFD alone does not account for the elasticity of the plates. To address this gap, Refs. 24–26 introduced a fully coupled hydroelastic CFD and computational solid mechanics (CSM) approach to simulate the fluid–structure interaction (FSI) between waves and a submerged horizontal plate. The present approach is developed in OpenFOAM, an open-source C++ framework for developing CFD-based solvers, and builds upon the initial finite-volume FSI framework of Refs. 27 and 28. This paper continues to investigate irregular waves (focused wave groups) interacting with a submerged horizontal plate, focusing on the nonlinear responses, which have not been previously explored using the CFD+CSM method.[29]

The hydroelastic responses to waves discussed in this paper will be crucial for directly determining stress, a key factor in calculating the fatigue of the submerged horizontal plate. Fatigue damage is a major concern for offshore structures, drawing significant attention from researchers and engineers. Cumulative fatigue damage, initially proposed by Palmgren and later developed by Miner, remains a challenging and unresolved issue.[30] Common methods for fatigue analysis include the spectral method, the deterministic method, and the time-domain analysis method based on the rainflow counting rule.[31,32]

The spectral method is a stochastic approach that assumes linear load and structural analysis, modeling short-term stress variations as a random narrow-banded stationary process following the Rayleigh distribution. However, this method is limited to narrow-band processes with bandwidth parameters less than 0.5.[33] In reality, the stress response of offshore structures is often wide-banded, leading to conservative fatigue damage estimates.[34] Researchers like Rice,[35] Wirsching and Light,[36] Benasciutti and Tovo,[37] and Braccesi *et al.*[38] have developed spectral bandwidth correction factors to mitigate this conservatism, but these formulas are complex and not always effective. For processes with bandwidth parameters greater than 0.5, the spectral method tends to overestimate fatigue damage.[33] The deterministic method simplifies the spectral method by characterizing wave-induced load effects using deterministic wave heights and periods, rather than stochastic variations.[39] While simpler, this method fails to capture the stochastic nature of sea waves. The time-domain analysis method uses coupled dynamic analysis to adequately consider nonlinearity in fatigue damage assessment. This method provides accurate fatigue damage predictions with the rainflow counting technique,[34] but it is computationally intensive and time-consuming.

These traditional methods have notable limitations. In this paper, a phase-decomposition method (detailed in Sec. III A) is used to cleanly separate each individual response harmonic of the plate, potentially overcoming these limitations by obtaining accurate and real harmonic components of the response.

In summary, this paper aims to fill a critical research gap by investigating the nonlinear response of submerged elastic plates interacting with waves. The objectives are to demonstrate two novel applications:

- This is the first numerical investigation of focused irregular wave interactions with elastic structures using a fully nonlinear CFD+CSM model.
- Since the method was initially introduced by Zang *et al.*[40] to successfully separate hydrodynamic force harmonics on a cylinder, this study represents the first effort to extend the phase-decomposition method to cleanly separate structural response harmonics.

Through these novel applications, the significance of nonlinear responses is analyzed in relation to various plate rigidities and relative plate lengths in Sec. IV. Moreover, the clean separation of response harmonics at specific frequencies from irregular wave interactions offers the potential for more efficient cumulative fatigue damage assessments in given sea states. This contribution, detailed in Sec. V, provides new insights for advancing fatigue analysis methodologies in offshore engineering applications.

II. METHODOLOGY

This paper uses the CFD+CSM model to solve fully nonlinear wave–elastic plate interactions. This section introduces the model, illustrates the numerical wave tank setup, and demonstrates verification and validation focusing on the wave-induced responses of a

06 January 2025 12:39:23

© Author(s) 2025

horizontal elastic plate to indicate the model's accuracy, supporting the following research.

A. Computational model

The present model couples two sub-regions: CFD and CSM. The fluid sub-region is simulated using the *interFOAM* solver. Waves are generated and dissipated via the relaxation-based wave generation toolbox, waves2Foam, as proposed by Jacobsen *et al.*[41] *interFOAM* utilizes the Navier–Stokes equations to describe two-phase flow, expressed through the mass conservation equation and the momentum equation according to Newton's second law,

$$\frac{\partial \rho}{\partial t} + \nabla \cdot (\rho \mathbf{u}) = 0, \tag{1}$$

$$\frac{\partial (\rho \mathbf{u})}{\partial t} + \nabla \cdot (\rho \mathbf{u}\mathbf{u}^T) = -\nabla P - (\mathbf{g} \cdot \mathbf{x})\nabla \rho + \nabla \cdot (\mu \nabla \mathbf{u}) + \sigma_t k_\gamma \nabla \gamma. \tag{2}$$

Here, $\mathbf{u} = (u, v, w)$ is the flow velocity vector, ρ is the fluid density, t represents time, $\mathbf{x} = (x, y, z)$ is the Cartesian coordinate vector, P is the pressure in excess of the hydrostatic part, $\mathbf{g}$ is gravity acceleration, μ is dynamic viscosity, and σ_t, γ, and k_γ are the surface tension coefficient, the volume fraction, and surface curvature, respectively. Both water and air are resolved using these equations.

The volume of fluid (VOF) method tracks the free surface's shape and position. The VOF field's transport equation is

$$\frac{\partial \gamma}{\partial t} + \nabla \cdot (\vec{U}\gamma) = 0, \tag{3}$$

where γ represents the volume fraction: 0 for air, 1 for water, and intermediate values for the interface mixture. An additional convective term sharpens the interface resolution, expressed as

$$\frac{\partial \gamma}{\partial t} + \nabla \cdot (\vec{U}\gamma) + \nabla \left[\vec{U}_\gamma \gamma (1-\gamma)\right] = 0. \tag{4}$$

Here, $\vec{U}_\gamma = \vec{U}_l - \vec{U}_\mathbf{g}$, with $\vec{U} = \gamma \vec{U}_l + (1-\gamma)\vec{U}_\mathbf{g}$, where $\vec{U}_l$ and $\vec{U}_\mathbf{g}$ denote the corresponding liquid and gas velocities, respectively. In simulations, two immiscible fluids are treated as one effective fluid, with properties like density and dynamic viscosity determined by weighted averages using γ,

$$\phi = \gamma \phi_{water} + (1-\gamma)\phi_{air}. \tag{5}$$

This method ensures physical properties equate to those of each fluid in their respective regions and vary only across the interface.

The solid sub-region is governed by the conservation of momentum, with stress described by the nonlinear St. Venant–Kirchhoff hyperelastic law as implemented by Cardiff *et al.*[28] The mathematical model in the total Lagrangian form (reference configuration) is expressed as

$$\oint \rho_{solid} \frac{\partial}{\partial t}\left(\frac{\partial \mathbf{u_d}}{\partial t}\right) \mathrm{d}V = \oint \mathbf{n} \cdot (\Sigma \cdot \mathbf{F}^T) \cdot \mathrm{d}S + \oint \rho_{solid} \mathbf{g} \mathrm{d}V, \tag{6}$$

where ρ_{solid} is the density of the solid structure, $\mathbf{u}_d$ is the displacement vector, $\mathbf{n}$ denotes the outward facing normal vector, $\mathbf{F} = I + (\nabla \mathbf{u}_d)^T$ is the deformation gradient tensor, I is the second-order identity tensor, and Σ is the second Piola–Kirchhoff stress tensor. The Cauchy stress tensor σ is related to Σ by

$$\sigma = \frac{1}{\det \mathbf{F}} \mathbf{F} \cdot \Sigma \cdot \mathbf{F}^T. \tag{7}$$

The stress–strain relationship for the submerged horizontal plate is given by

$$\Sigma = 2G\mathbf{S} + \Lambda tr(\mathbf{S})I, \tag{8}$$

where the Green–Lagrange strain tensor is

$$\mathbf{S} = \frac{1}{2}\left[\nabla \mathbf{u}_d + (\nabla \mathbf{u}_d)^T + \nabla \mathbf{u}_d \cdot (\nabla \mathbf{u}_d)^T\right]. \tag{9}$$

Here, G and Λ are the Lamé's coefficients, related to Young's modulus E and Poisson's ratio ν by

$$G = \frac{E}{2(1+\nu)}, \tag{10}$$

$$\Lambda = \frac{\nu E}{(1+\nu)(1-2\nu)}. \tag{11}$$

The coupling between the CFD and CSM solvers in this study is achieved using a partitioned scheme, as proposed by Tuković *et al.*[27] In this approach, the fluid and solid solutions are computed alternately, with the kinematic and dynamic conditions at the fluid–solid interface iteratively matched. Specifically, a Dirichlet–Neumann coupling procedure is employed, in which the velocity and pressure fields are solved in the fluid domain, with the interface forces transferred to the solid domain as boundary conditions. The structural displacement is then computed in the solid domain and used to update the boundary conditions on the fluid side. These steps are repeated until the kinematic and dynamic conditions at the interface are fully satisfied.

To enhance the efficiency of the coupling, the Aitken relaxation method is implemented, adjusting the relaxation factor (ARF) dynamically based on the residual between the structural interface displacement (SID) and the fluid interface displacement (FID). The ARF is updated as follows:

$$\mathrm{ARF}_{i+1} = \mathrm{ARF}_i \times \left[1 - \frac{\sum(Res \cdot \Delta Res)}{\sum(\Delta Res \cdot \Delta Res)}\right]. \tag{12}$$

Here, $Res = \mathrm{SID} - \mathrm{FID}$ represents the residual displacement at the interface, and ΔRes is its change between iterations. This updated ARF is then used to adjust the fluid mesh according to

$$\mathrm{Fluid\ Mesh}_{i+1} = \mathrm{Fluid\ Mesh}_i + \mathrm{ARF} \times Res. \tag{13}$$

After updating the mesh, the fluid solver calculates the velocity and pressure fields, providing the interface forces as inputs to the structural solver. The structural solver then computes the displacement, which is used to update the interface residual. This process continues iteratively within each time step until the residual falls below a specified threshold (1×10^4 m in this study, as recommended by Huang *et al.*[25]).

The entire coupling process, summarized in Fig. 1, ensures accurate interaction between the fluid and structural solvers, enabling the simulation of complex fluid-structure interaction phenomena, including nonlinear deformations.

B. Numerical wave tank setup

A rectangular fluid domain is established in a two-dimensional Cartesian x-y coordinate system, as illustrated in Fig. 2. The

06 January 2025 12:39:23

© Author(s) 2025

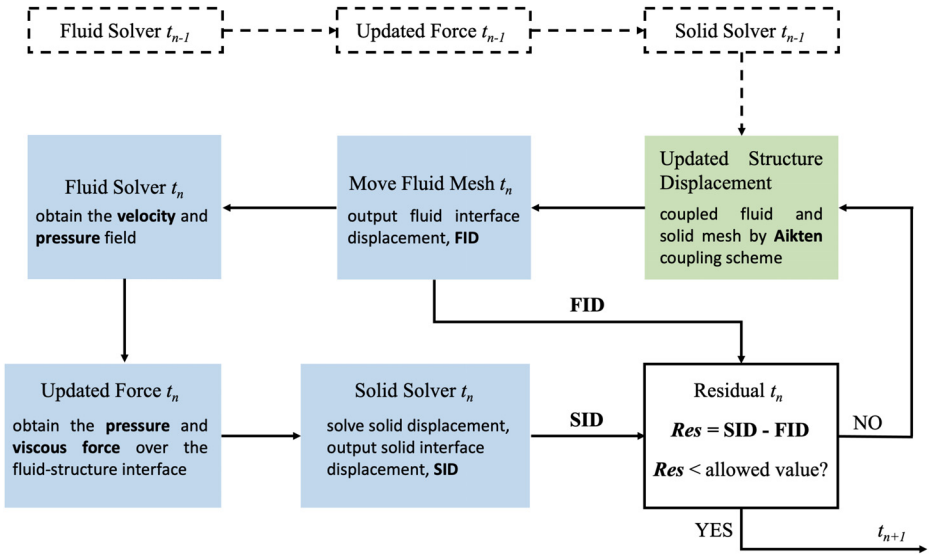

FIG. 1. Flowchart of the fluid–structure interaction procedure.

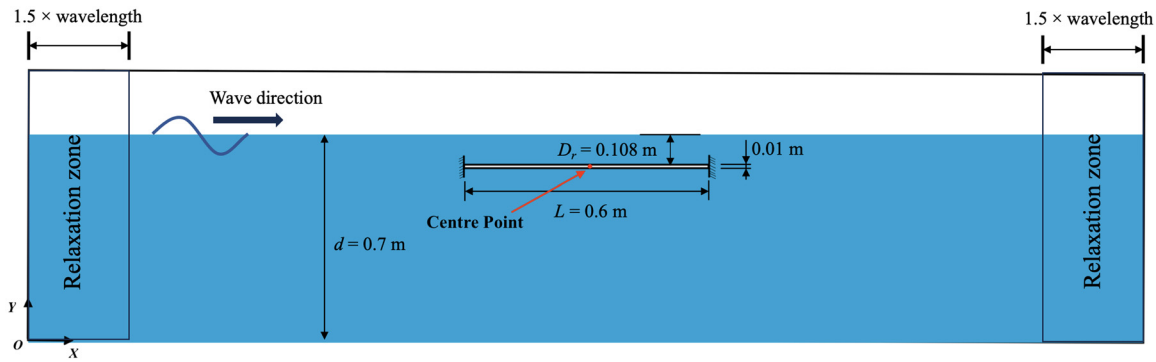

FIG. 2. Numerical wave tank. The submerged horizontal plate has the deformable upper and lower boundaries and fixed left and right boundaries as restraints.

computational domain is assumed to be two-dimensional (i.e., uniform in the spanwise direction) based on the condition that the submerged horizontal plate, acting as a VLFS, is side-mounted and spans extensively in the profile direction, with incoming waves propagating uni-directionally along the x-axis.

In the numerical wave tank (Fig. 2), the submerged horizontal plate is centrally positioned, featuring relaxation zones at both the inlet and outlet boundaries to effectively manage wave reflections. The inlet boundary's relaxation zone is designed to absorb waves reflected from the plate, while the outlet boundary's relaxation zone mitigates wave reflections. Following recommendations by Jacobsen *et al.*,[41] each relaxation zone extends 1.5 × the wavelength of the incident waves to ensure complete wave attenuation.

The computational domain is two-dimensional, with the front and back boundaries specified as "empty," eliminating variations in the third dimension. The bottom boundary, representing the seabed, is assigned a "wall" condition, enforcing a no-slip boundary with zero fluid velocity to simulate interactions between the waves and the sea floor. The top boundary, representing the atmosphere, is designated as a "patch," facilitating accurate modeling of the air–water interface and capturing free surface interactions.

The plate is submerged beneath the free surface. Similar dimensions to those used in Ref. 26 on a submerged horizontal plate breakwater were selected for the present tests. The vertical distance from the plate to the still water level is 0.108 m, with the plate's length and thickness being 0.6 and 0.01 m, respectively. The density of the plate is kept at 1000 kg/m^3, and Poisson's ratio is 0.3. The Young's modulus, representing the plate's rigidity, will be varied and discussed in subsequent sections. The boundary conditions for the plate are set to ensure accurate modeling of its structural response. The left and right edges of the plate are clamped, with the boundary condition in OpenFOAM specified as "fixed displacement." The top and bottom surfaces of the plate are fully flexible, with the boundary condition specified as "solid traction." These clamped edge conditions provide strong support to maintain the plate's position, while the flexible surfaces allow for realistic deformation. This research focuses on the displacement at the center point of the plate, as highlighted in Fig. 2.

06 January 2025 12:39:23

© Author(s) 2025

The mesh layout used in the present computational process is shown in Fig. 3. Both the fluid and solid sub-regions are discretized into mesh cells. The fluid sub-region is represented by light blue mesh cells, as typically seen in OpenFOAM test cases, while the solid plate is represented by yellow mesh cells for the CSM solutions. The mesh size is determined based on previous mesh convergence tests. According to Ref. 42, for accurate two-dimensional wave–structure interaction in OpenFOAM, the horizontal mesh size (x-axis) should be $\Delta x = L_w/200$, where L_w is the incoming wavelength. The vertical mesh size (y-axis) should be $\Delta y = H_w/10$, where H_w is the incoming wave height. For accurate CSM solutions, the mesh size is defined based on the convergence test in Ref. 26, with $\Delta x = 0.005$ m and $\Delta y = 0.0025$ m for a plate of the same size.

Focused waves are a short-term type of irregular waves that swiftly increase in amplitude from a moderate level to a peak, matching the average shape of the largest events in a random time series.[43,44] In this research, we generate and analyze focused wave groups based on NewWave theory, targeting the center point of the plate as the focus point. These waves are generated using the JONSWAP spectrum with an enhancement factor of 3.3. Two peak wave periods, 1.2 and 1.4 s, are selected for this research, with a water depth of 0.7 m. These wave conditions, scaled at 1/100, are considered reasonable for sea states.[45] The main crest wave amplitude for both wave periods is 0.05 m. Before conducting wave–structure interaction tests, the waves are generated in an empty tank to ensure a proper focused shape and accurate main crest wave amplitude. Figure 4 shows the free surface elevations of focused waves at the targeted focus location (i.e., the planned center point of the plate) in the empty tank.

In addition to the wave conditions, the parameters considered in this study are summarized in Table I. Two incident wave periods are employed to characterize the relative plate length to wavelength, denoted as kL, where k is the wave number and L is the plate length. For each relative plate length, five different Young's moduli are tested to represent varying plate rigidities. The dimensionless plate rigidity is expressed as $\beta = \frac{D}{\rho g L^4}$, where $D = \frac{Eh^3}{12(1-\nu^2)}$ is the flexural rigidity of the

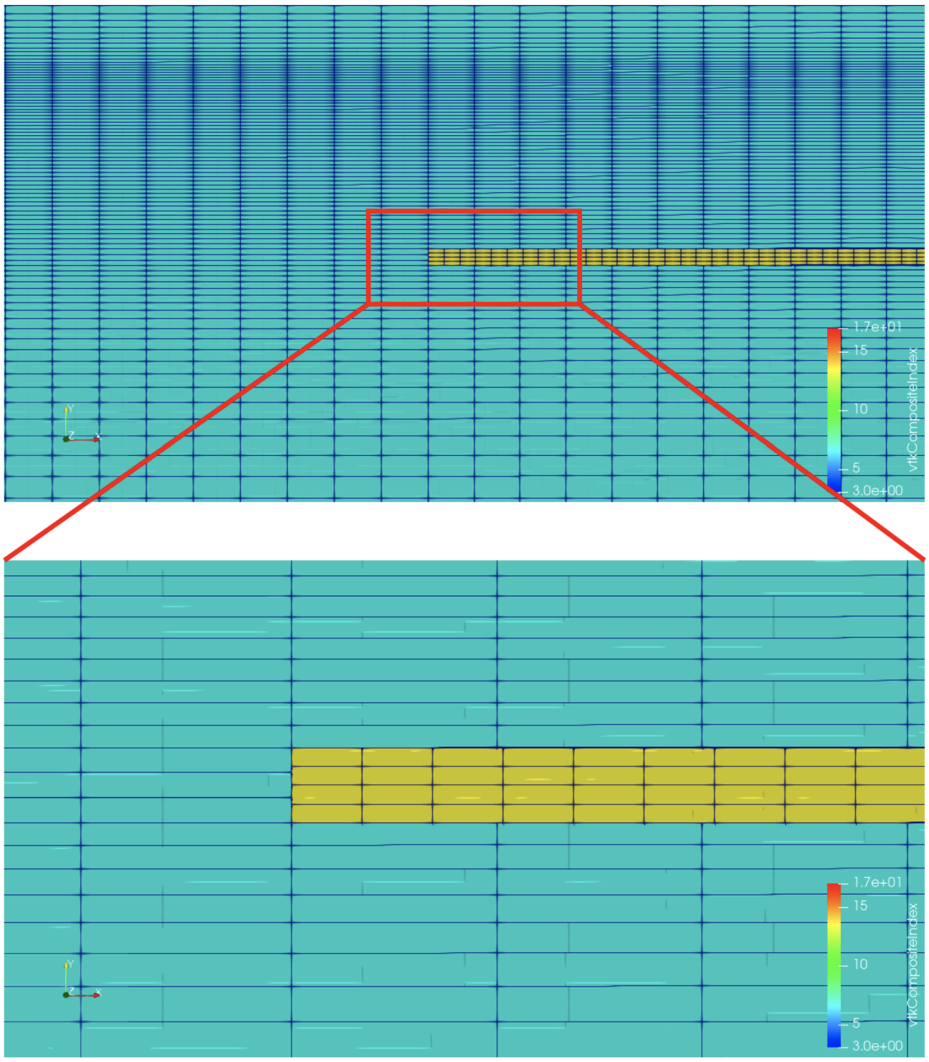

FIG. 3. Mesh layouts of the model around the left edge of the plate with light blue denoting fluid mesh and yellow denoting solid mesh.

06 January 2025 12:39:23

© Author(s) 2025

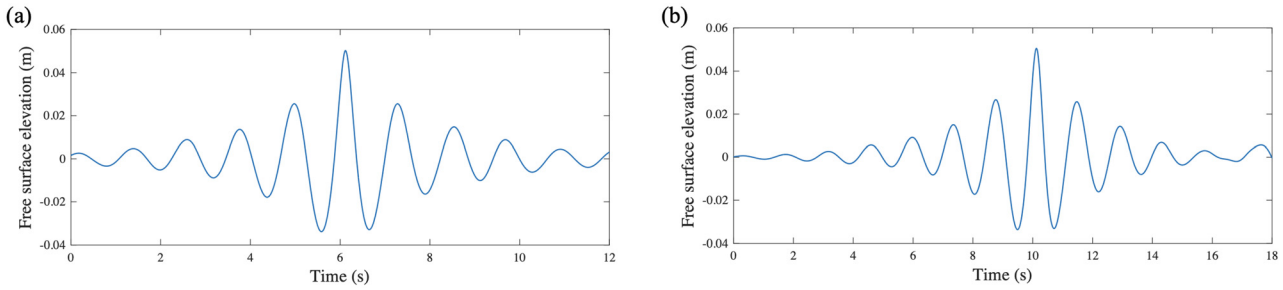

FIG. 4. Free surface elevations of incident focused wave groups at the focused location in the empty tank: [left panel (a)] for a peak wave period of 1.2 s and [right panel (b)] for a peak wave period of 1.4 s.

TABLE I. Test conditions including wave periods, relative plate length to wavelength (kL), Young's modulus, and dimensionless plate rigidity (β).

Case group No.	Incident wave period	Relative plate length to wavelength (kL)	Young's modulus (MPa)	Dimensionless plate rigidity (β)
1	1.4 s	1.344	25	18
2			50	36
3			75	54
4			100	72
5			250	180
6	1.2 s	1.736	25	18
7			50	36
8			75	54
9			100	72
10			250	180

plate, ρ is the fluid density, g is the gravity acceleration, h is the plate thickness, and ν is the Poisson's ratio. In total, ten groups of cases are analyzed in this study, with each group comprising two test cases for crest- and trough-focused waves.

C. Verification and validation

To support the following investigations of the center point displacement of the plate based on the CFD+CSM model, it is necessary to validate the numerical model's predictions of the point displacement of an elastic plate. Sree *et al.*[46] reported measurements of wave-induced deformations of a similar horizontal plate, which was free of restraints at both the left and right edges and placed at the water surface. Therefore, the experiment by Sree *et al.*[46] was reproduced to validate the accuracy of the present computational approach in modeling plate deformation and point displacement in waves. The experimental conditions were a wave period of $T = 0.7$ s and a wave height of $H = 0.017$ m. The plate was 1 m long and 0.01 m thick, with rheological properties of density $\rho = 910\,\mathrm{kg/m^3}$, Young's modulus $E = 870$ MPa, and Poisson's ratio $\nu = 0.3$. In this physical experiment, a regular wave was used, and the plate was free to deform without restraints.

In the CFD+CSM simulations, a constant time step is applied to all test cases. While mesh convergence tests for similar setups have been conducted in our previous work for both the fluid solver in CFD[42] and the solid solver in CSM,[26] time step convergence tests are necessary to ensure the accuracy of the CFD+CSM simulations. The mesh configuration used in this study is consistent with the setup described in Sec. II B, which was validated in earlier mesh convergence tests. The time step convergence tests are conducted based on the validation case setup. Figure 5(a) presents the time histories of displacement for the point located 0.1 m away from the left edge of the plate, simulated using three different time steps: $\Delta t = 0.002$, 0.001, and 0.0005 s. The computational time required to simulate a real-time duration of 8 s for these three time steps is 34.5, 40.2, and 55.7 h, respectively. The displacement results for a time step of 0.002 s show noticeable discrepancies in both the crest and trough of the curves when compared to the results for time steps of 0.001 and 0.0005 s. However, the results obtained with a time step of 0.001 s converge closely to those obtained with a time step of 0.0005 s. Considering the balance between computational accuracy and time efficiency, a constant time step of 0.001 s is employed for all subsequent simulations in this study.

As shown in Fig. 5(a) for the point 0.1 m away from the left edge, the displacement of points on the plate was linear. Thus, wave-induced deformations can be represented by the amplitude value of the linear sinusoidal curve peak. These deformations, in terms of non-dimensional vibration amplitudes (point displacement amplitude divided by its thickness), were measured over the plate, as presented in Fig. 5(b). The present CFD+CSM model simulation results show good agreement with both the experimental data from Ref. 46 and previous numerical results from Ref. 26. This validation case demonstrates a linear response due to the small incident wave amplitude and the absence of restraint. Although nonlinear validation cases are not presented

06 January 2025 12:39:23

© Author(s) 2025

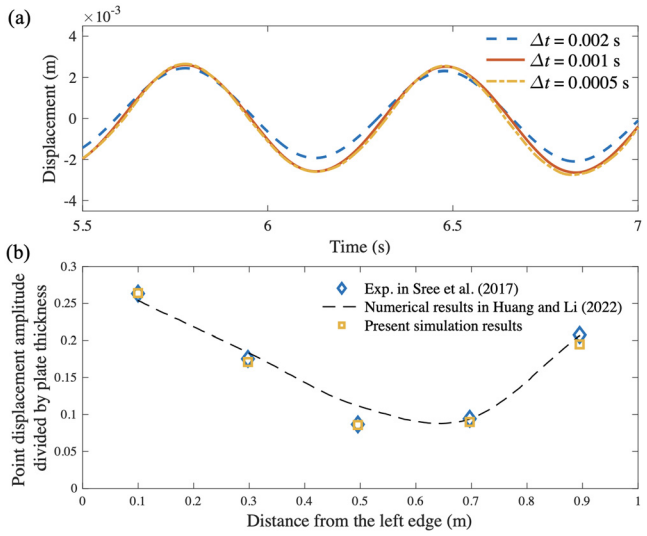

FIG. 5. [Top panel (a)] Convergence test results for the time step of displacement at the point 0.1 m from the left edge of the plate in time histories. [Bottom panel (b)] Normalized displacement amplitude along the plate length, comparing experimental measurements with numerical simulations.

here, Huang and Li[26] successfully employed the CFD+CSM model under more severe wave–structure interaction conditions, where nonlinearities were captured. This provides strong evidence that the model can reliably simulate the nonlinear interactions explored in the following research.

III. SPECTRAL DECOMPOSITION

A phase-decomposition method is introduced in this section to separate the responses. An example case is used to demonstrate the separation results.

A. Phase-decomposition method

The interaction under consideration involves the diffraction of a unidirectional incident focused wave by a structure. According to the classic Stokes perturbation expansion cited in Ref. 47, the hydrodynamic load can be formulated as follows:

$$F = Af_{11}\cos\varphi + A^2(f_{20} + f_{22}\cos 2\varphi) + A^3(f_{31}\cos\varphi + f_{33}\cos 3\varphi) + A^4(f_{42}\cos 2\varphi + f_{44}\cos 4\varphi) + O(A^5). \quad (14)$$

In this formulation, wave loads are decomposed into a fundamental component that aligns closely with the spectral peak frequency of the incident waves, along with higher harmonics of this primary frequency. These higher harmonics occur at frequencies close to integer multiples of the fundamental frequency due to nonlinearity in both the incident waves and the wave–structure interactions. The load is developed up to the fourth order in amplitude A, where the coefficients f_{mn} are wave-to-force transfer functions. The phase of the linear component of the incident wave, represented as, $\varphi = \omega_\varphi t + \varphi_0$, includes a prescribed phase shift φ_0. To simplify the force expression, the term $f_{mn}\cos n\varphi$ represents $Re(f_{mn}e^{in\varphi + i\psi_{mn}})$, where ψ_{mn} is the phase shift of the force relative to incident wave at a given order and harmonic. Notably, the terms multiplying the coefficients f_{mn} denote the power of the amplitude term is the same as the frequency harmonic, while the terms multiplying coefficients such as $f_{(m(m-2))}$ refer to the power of the amplitude exceeds that of the frequency harmonic by 2.

To investigate the point displacement of the horizontal plate, focusing on the center point, we consider the individual harmonics. Each harmonic has a specific frequency, and the point displacement follows the frequency domain governing equation of motion,

$$(-\omega^2(M + \mu_0) - i\omega\lambda + K)Z = F. \quad (15)$$

In this equation, ω is the angular frequency of vibration, M is the mass, and μ_0 is the added mass. The term λ denotes the damping coefficient, which is correlated with the displacement Z and can be expressed as a function $\lambda(Z)$. The parameter K represents the buoyancy stiffness, and F is the total external force, including wave radiation and wave excitation forces.

Although the damping term λ varies, it primarily affects the amplitude rather than the frequency of phase terms. Thus, the displacement response, even under varying damping, can be accurately modeled using this perturbation expansion. This approach reflects the complex interplay between the applied force and the resulting vibratory motion of the plate. By applying the Stokes-type expansion to the displacement, we obtain

$$Z = A\zeta_{11}\cos\varphi + A^2(\zeta_{20} + \zeta_{22}\cos 2\varphi) + A^3(\zeta_{31}\cos\varphi + \zeta_{33}\cos 3\varphi) + A^4(\zeta_{42}\cos 2\varphi + \zeta_{44}\cos 4\varphi) + O(A^5). \quad (16)$$

Here, ζ_{mn} are the displacement coefficients corresponding to the force coefficients f_{mn}. These coefficients represent the transfer functions from the applied force to the resulting displacement, capturing both the amplitude and phase of each harmonic component.

Building on the generalized Stokes-type harmonic series, Zang *et al.*[40] and Chen *et al.*[48] successfully extracted higher force harmonics in their interactions using a two-phase decomposition method. Similarly, the displacement Z can be decomposed as follows:

$$\frac{(Z_0 + Z_{180})}{2} = A\zeta_{11}\cos\varphi + A^3(\zeta_{33}\cos 3\varphi + \zeta_{31}\cos\varphi) + O(A^5), \quad (17)$$

$$\frac{(Z_0 - Z_{180})}{2} = A^2(\zeta_{20} + \zeta_{22}\cos 2\varphi) + A^4(\zeta_{44}\cos 4\varphi + \zeta_{42}\cos 2\varphi) + O(A^6). \quad (18)$$

This method, utilizing the point displacement under crest-focused waves (Z_0) and trough-focused waves (Z_{180}), enables the separation of odd and even harmonics.

B. Individual point displacement harmonic

The test case with a submerged horizontal plate having a dimensionless plate rigidity, $\beta = 18$, and a relative plate length, $kL = 1.344$, interacting with focused wave groups, with a peak wave period of 1.4 s and a main crest amplitude of 0.05 m, is used as an example for the separation of individual point displacement harmonics.

Figure 6(a) shows the time histories of the center point displacement of the plate interacting with crest- and trough-focused waves, corresponding to Z_0 and Z_{180} in Eq. (15). By utilizing the two-phase method, the odd and even harmonics can be separated, as shown in

06 January 2025 12:39:23

© Author(s) 2025

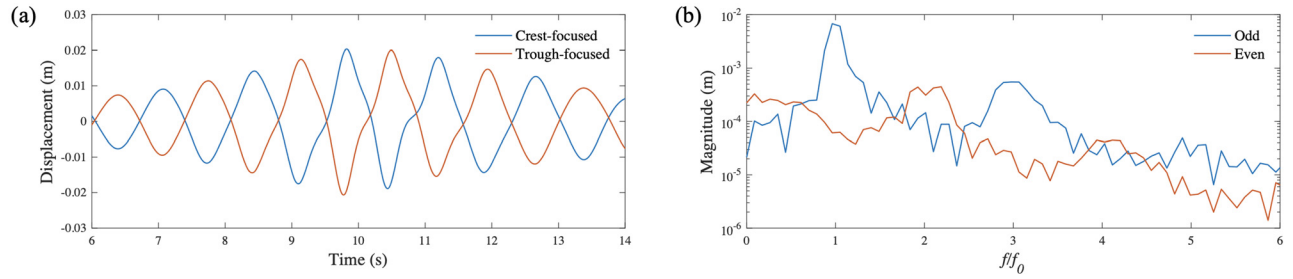

FIG. 6. [Left panel (a)] Time histories of center point displacement for crest- and trough-focused waves. [Right panel (b)] Displacement magnitude spectra showing separated harmonic components using the two-phase method.

the amplitude-frequency spectra in Fig. 6(b). This method ensures that the first-order harmonics, for example, are not influenced by neighboring harmonics such as the zeroth-order and second-order harmonics. The inherent overlapping between these harmonics is effectively separated.

Using the inverse fast Fourier transform (IFFT) for each harmonic in the frequency domain, individual point displacement harmonics can be obtained in time histories, as shown in Fig. 7 from the first to the fifth harmonics. In addition to the time–displacement curves shown in Fig. 7, the envelopes are also presented to reflect the correlations between the linear component and nth-order harmonics, similar to those in Ref. 48 for wave forces. The envelope of the linear component is directly obtained from the Hilbert transform of the linear time–displacement curve. The envelopes of nth-order harmonics from the second-order onward are obtained by raising the fundamental envelope to the power of n and scaling by a least squares method to match the maximum value of the nth-order time–displacement curve. The estimated nth-order harmonic envelopes based on the linear envelope in Fig. 7 well encapsulate the time–displacement curves, indicating that the displacement harmonics follow specific correlations between linear and nth-order harmonics, similar to wave forces in Ref. 48 for this example case.

IV. NONLINEAR POINT DISPLACEMENT

The visualizations in Fig. 8 show the deformations of the two-edge-clamped submerged horizontal plate with $\beta = 36$ and $kL = 1.344$ when the focused wave group in Fig. 4(b) interacts with it during the numerical simulations. The displacement at the center point is observed to be the largest deformation and can be used to calculate the critical vertical stress in Secs. IV A–IV C. Therefore, in the subsequent parts of this section, only the center point will be discussed.

Using the phase-decomposition method, the time histories of the center point displacement can be utilized to define the peak displacement amplitude at each individual harmonic. This allows for the discussion of the significance of the nonlinear components. The influence of two parameters, plate rigidity and relative plate length, are examined and discussed.

A. Influence of plate rigidity

Five different dimensionless plate rigidities β are compared, as shown in Fig. 9. All cases involve interactions with focused waves having a wave period of 1.4 s and a main crest wave amplitude of 0.05 m. The time–frequency contour plots in Fig. 9 are obtained by wavelet transform to show the magnitude of the center point displacement over time and the ratio of frequency to the incident wave peak frequency (f/f_0, where $f/f_0 = n$ refers to the *nth* harmonic). In these contour plots, the color bar changes from dark blue to green to dark red as the magnitude increases from 0 to the peak value. The dark red

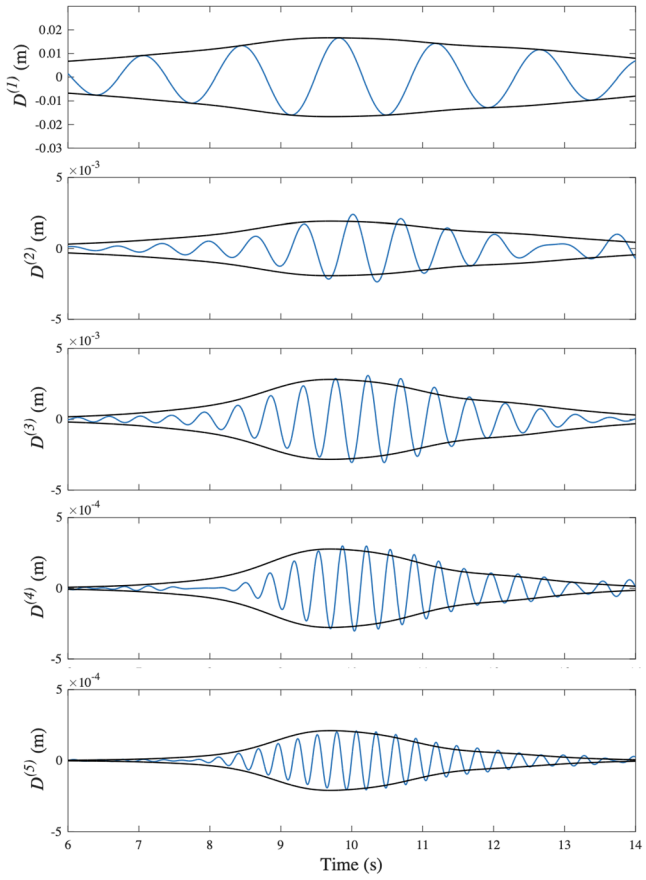

FIG. 7. Time histories of each individual displacement harmonic decomposed by the two-phase method alongside its envelope for a plate with $\beta = 18$ and $kL = 1.344$.

06 January 2025 12:39:23

© Author(s) 2025

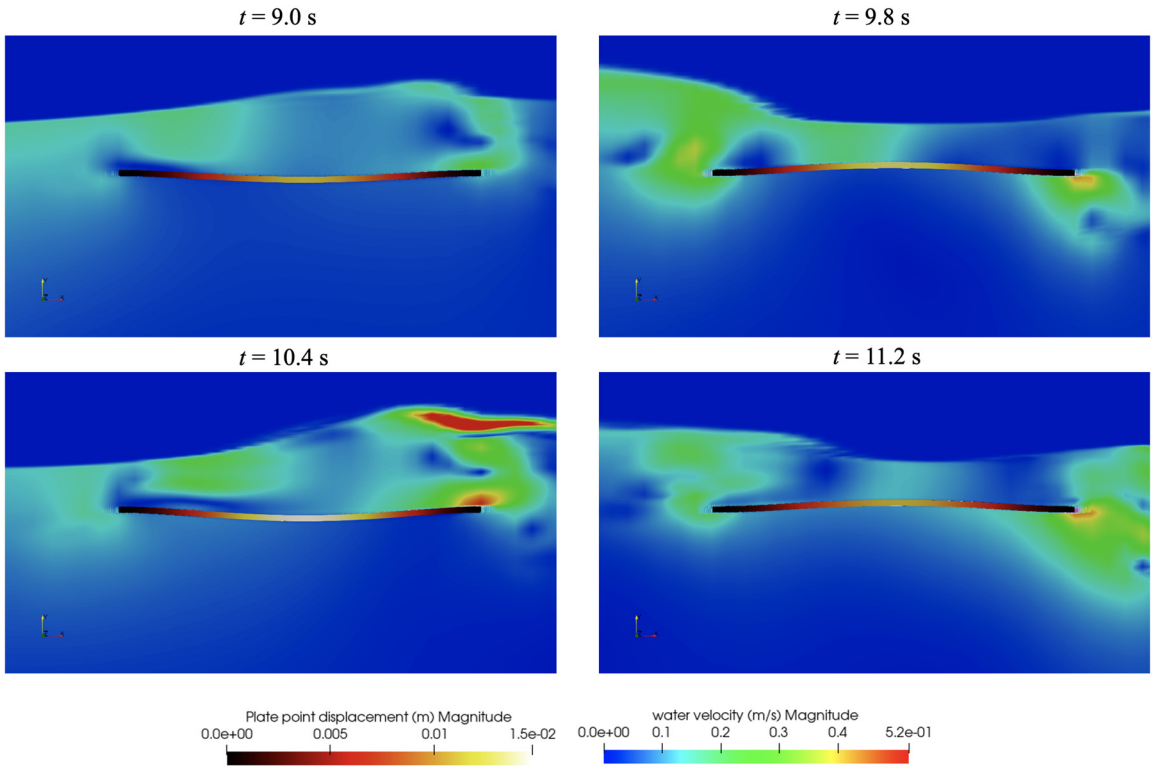

FIG. 8. Snapshots of the visualized numerical simulations of the deformation of a submerged horizontal plate with Young's modulus of 50 MPa interacting with the focused wave group in Fig. 4(b). The time t in these snapshots corresponds to the time point reflected in the time histories presented in Fig. 4(b).

areas always occur around the focused time at 10 s and at the linear components (i.e., first-order harmonics).

As the value β increases from 18 in Fig. 9(a) to 54 in Fig. 9(c), the higher-order harmonics become dark red, indicating a higher proportion relative to the linear components. However, as the value of β continues to increase from 54 in Fig. 9(c) to 180 in Fig. 9(e), the colors at higher-order harmonics turn back to light blue, indicating a decreased proportion relative to the linear components.

Alongside the time–frequency contour plots, the time histories of the center point displacement are also plotted as red curves. These time–displacement curves also reflect the same changes in nonlinear components. In Fig. 9(a), the time–displacement curves follow the peak incident wave frequency, indicating that the linear components dominate the displacement. As the value of β increases, the time–displacement curves in Figs. 9(b) and 9(c) show significant higher-frequency wiggles. In the larger plate rigidity cases in Figs. 9(d) and 9(e), these wiggles gradually become smaller.

It is also noted that these nonlinear higher-frequency wiggles become more significant after the main crest of the curves. In the time–frequency contour plot, the larger magnitude regions at higher frequencies do not symmetrically distribute based on the incident wave focus time at 10 s like linear component, but occur after 10 s. This suggests that the linear components are mainly induced by the external waves, while the relatively large higher-order harmonics may also be influenced by other factors, such as structural resonance.

Using the two-phase decomposition method, the time–displacement curves for each individual harmonic, along with their envelopes, are obtained as shown in Fig. 10 for $\beta = 36$ and 54, and in Fig. 11 for $\beta = 72$ and 180. For the linear components, which are mainly induced by external waves, the wave-induced center point displacement monotonously decreases with the increasing Young's modulus, corresponding to a more rigid plate.

For the nonlinear components (the higher harmonics), unlike the case with $\beta = 18$ in Sec. III B, the wiggles for some higher harmonics are too broad for their approximated envelope, and the peak displacement does not align well with the peak of the estimated envelope obtained by raising the linear envelope to the corresponding *nth* power. This mismatch is considered to be due to structural resonance induced by the natural frequencies of the submerged plate. The significant nonlinear magnitudes observed in Fig. 9 indicate that structural resonance occurs at or around the natural frequencies.

The changes in the nonlinear proportion with varying plate rigidities, as observed in Fig. 9, indicate that the case with $\beta = 18$ has the least influence from structural resonance. Consequently, the higher harmonic time–displacement curves can be well encapsulated by the envelopes estimated from the linear envelope, indicating similar correlations between linear and higher harmonics as wave forces. In contrast, the other cases, affected by structural resonance, do not follow these correlations. However, for some harmonics less affected by structural resonance, such as the second harmonics in Figs. 10(b), 11(a),

06 January 2025 12:39:23

© Author(s) 2025

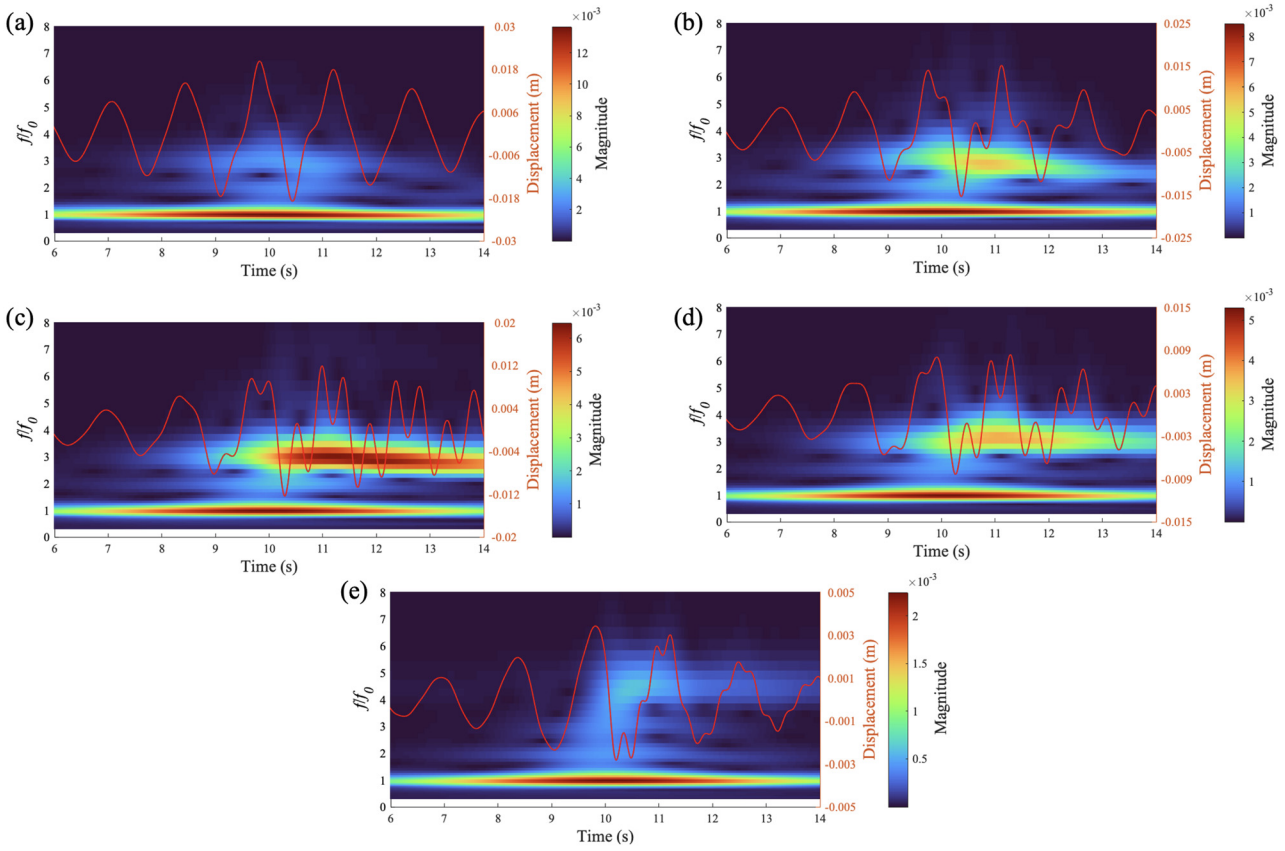

FIG. 9. Contour plots of center point displacement magnitude over frequency (where f_0 is the peak incident wave frequency) and time for a plate with dimensionless plate rigidity β of (a) 18, (b) 36, (c) 54, (d) 72, and (e) 180 interacting with waves having a peak wave period of 1.4 s.

and 11(b), and the third harmonics in Fig. 11(b), which are mainly induced by external wave loads, these correlations still hold well.

Additionally, from the observations in Figs. 10 and 11, it is evident that the influence of structural resonance covers not only a single harmonic but also a wider range of frequencies. The occurrence frequencies of structural resonance increase with the increase in β, which theoretically corresponds to the fact that more rigid structures have higher natural frequencies.

B. Influence of relative plate length

The time–frequency contour plots are shown in Fig. 12 for dimensionless plate rigidity β of 36 and 54 with the relative plate length to wavelength $kL = 1.344$ and 1.736, and in Fig. 13 for β of 72 and 180 with the relative plate length to wavelength $kL = 1.344$ and 1.736. The magnitude of the center point displacement in Figs. 12 and 13 is obtained over time and frequency using wavelet transform. This allows for a direct comparison of the occurrence of each individual harmonic for kL of 1.344 and 1.736 at specific frequencies. The linear displacement harmonics when $kL = 1.736$ and 1.344 can be observed at frequencies of 0.83 and 0.71 Hz, respectively. However, the higher-order harmonics influenced by structural resonance at a specific plate rigidity do not vary with kL. In Fig. 12, the cases with $kL = 1.344$ show a larger nonlinear component proportion relative to linear components (indicated by darker red around resonance frequencies). Conversely, when the value of β increases to 72 and 180 in Fig. 13, the cases with $kL = 1.736$ show a larger nonlinear component proportion relative to linear components.

The time–displacement curves in Fig. 14 for β of 54, Fig. 15 for β of 72, and Fig. 16 for β of 180 when $kL = 1.344$ and 1.736 are obtained using the two-phase decomposition method. From the parallel comparisons with the same y-axis scale in each figure, linear displacement, mainly induced by incident waves, shows negligible differences with the same amplitude. However, higher-order harmonics, influenced not only by the incident waves but also by resonance, exhibit more noticeable differences. Figures 12 and 13 indicate that resonance frequencies, which are due to natural frequencies, occur around a specific frequency that does not vary with the incident waves. Consequently, the resonance frequency when $kL = 1.736$ is close to the second-order harmonics, while it is closer to the third-order harmonics when $kL = 1.344$. This results in significantly larger third-order harmonic displacement in Fig. 14(b). The mismatch between the second-order harmonics and the second-order envelope is less pronounced than that in Fig. 14(a). Similarly, the fourth-order and fifth-order harmonics in Fig. 15 and the fifth-order harmonic in Fig. 16 also show significantly larger displacements.

06 January 2025 12:39:23

© Author(s) 2025

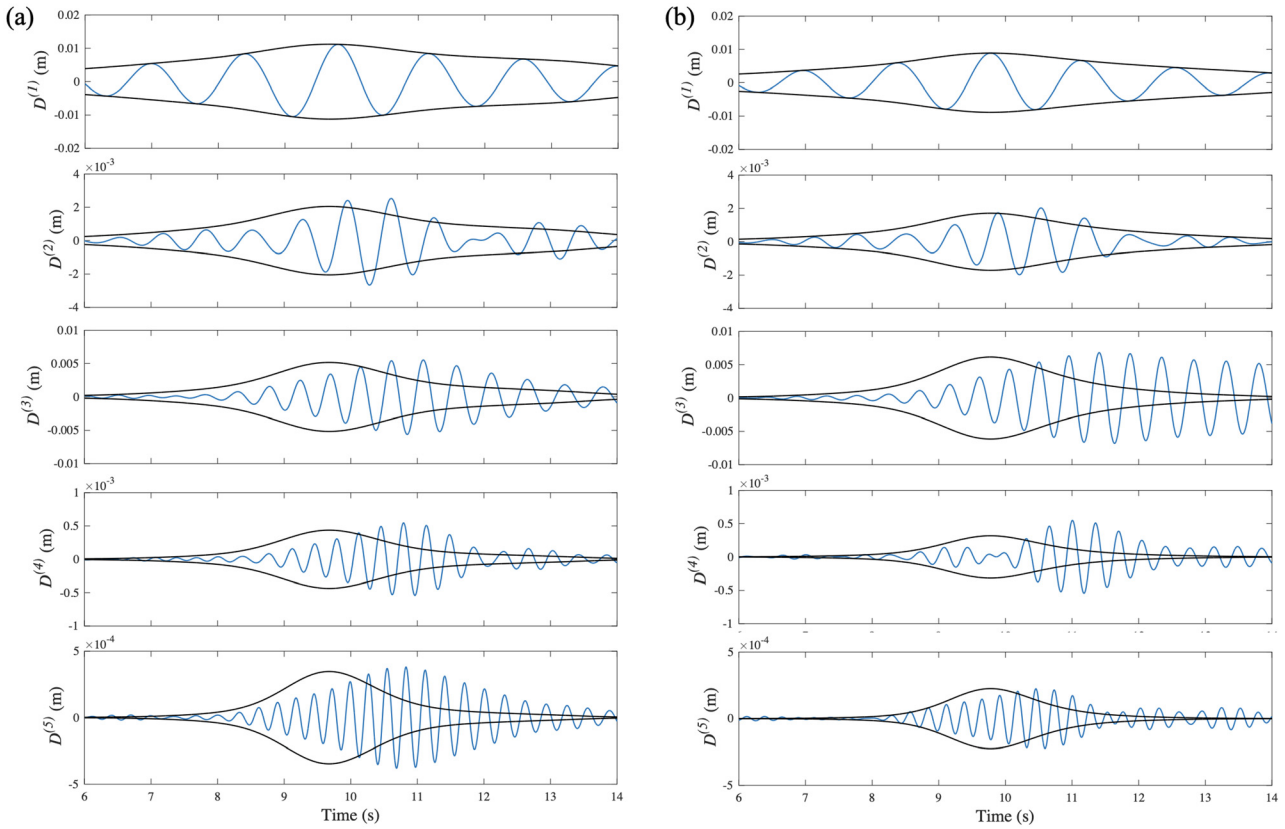

FIG. 10. Time histories of each individual displacement harmonic decomposed by the two-phase method alongside its envelope for a plate with dimensionless plate rigidity β of (a) 36 and (b) 54 interacting with waves having a peak wave period of 1.4 s.

The reduction in the nonlinear component proportion at the resonance region in Fig. 13 is due to the influences of resonance in different order harmonics. In all the cases when $kL = 1.736$ and in some cases when $kL = 1.344$ but with smaller β value, the enhancement of the higher-order harmonics amplified by resonance occurs around the second- and third-order harmonics. However, with larger β value, when $kL = 1.344$, the resonance primarily influences the fourth- and fifth-order harmonics. As the order of the harmonic increases, the displacement induced by resonance decreases. Consequently, in the time–frequency contour plots in Fig. 13, cases when $kL = 1.344$ show smaller values around the resonance region. This trend is more evident in Fig. 15.

C. Proportion of individual nonlinear point displacement harmonics

Even though the displacements due to structural resonance do not always follow the same correlations as wave forces between linear and higher harmonics, each individual displacement harmonic can be cleanly separated in the time histories without interference from wiggles at other frequencies. This clean separation enables the precise identification of the peak amplitude from the crest of each individual harmonic time–displacement curve. To quantitatively assess the significance of the nonlinear components, we calculate the ratio of the *nth*-order harmonic to the linear component, referred to as the *nth*-order ratio. These ratios are presented in Table II and visualized in Fig. 17, showing the proportion of each individual displacement harmonic relative to the linear component for varying plate rigidities and relative plate lengths.

Regarding the influence of dimensionless plate rigidity (β) on the significance of the nonlinear components, Table II indicates that the second harmonic consistently exhibits a significant proportion across all plate rigidities, with ratios exceeding 10% of the linear component when the relative plate length kL is 1.344. For $\beta = 54$, structural resonance causes the third harmonic to achieve the largest single-frequency nonlinear proportion, at 76.63% of the linear component. As natural frequency increases, when $\beta = 180$, the fourth-order harmonic ratio reaches 21.64%.

Figure 17 compares the proportions of *nth*-order displacement harmonics for two relative plate lengths. These results align with the discussions in Sec. IV B. The discrepancies in proportions between different kL values are attributed to structural resonance. When $\beta = 72$ and $\beta = 180$, structural resonance occurs at higher-order harmonics, where the influence of resonance diminishes as the harmonic order increases. Consequently, the nonlinear proportions remain similar for the two relative plate lengths. However, when $\beta < 72$, structural

06 January 2025 12:39:23

© Author(s) 2025

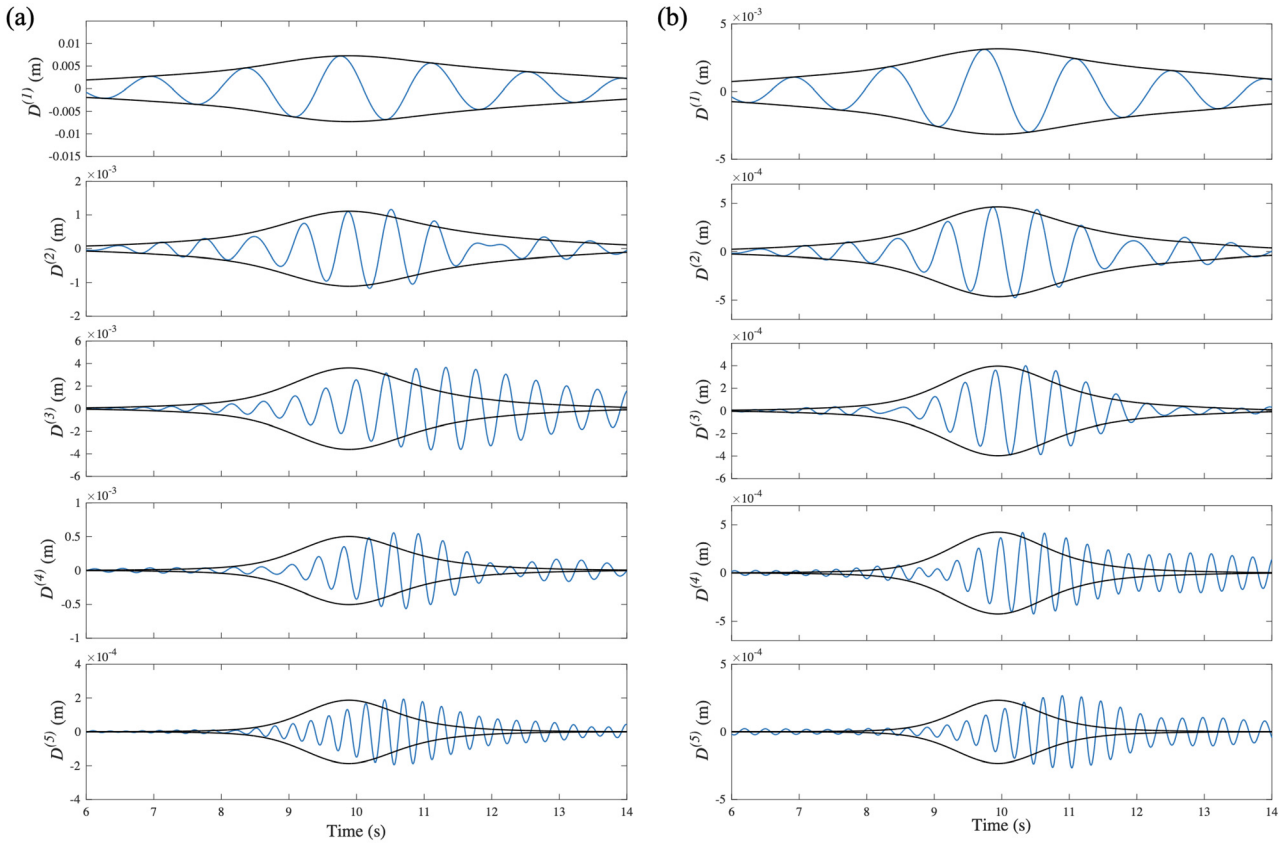

FIG. 11. Time histories of each individual displacement harmonic decomposed by the two-phase method alongside its envelope for a plate with dimensionless plate rigidity β of (a) 72 and (b) 180 interacting with waves having a peak wave period of 1.4 s.

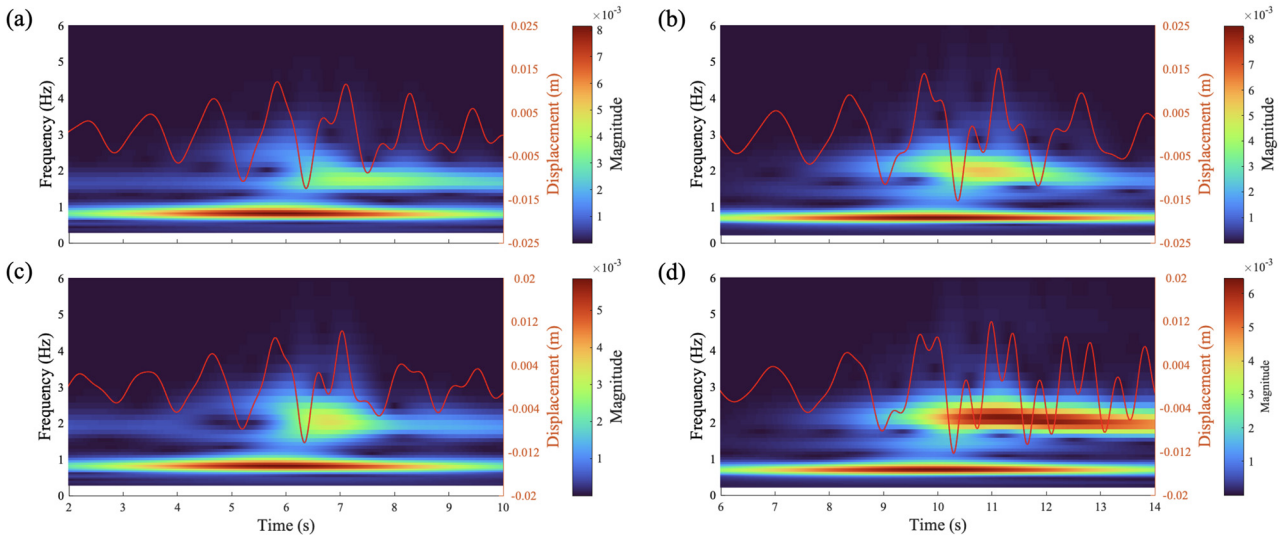

FIG. 12. Contour plots of center point displacement magnitude over frequency and time for a plate with dimensionless plate rigidity β of 36 when relative plate length kL of (a) 1.736 and (b) 1.344, and a plate with β of 54 when kL is of (c) 1.736 and (d) 1.344.

06 January 2025 12:39:23

© Author(s) 2025

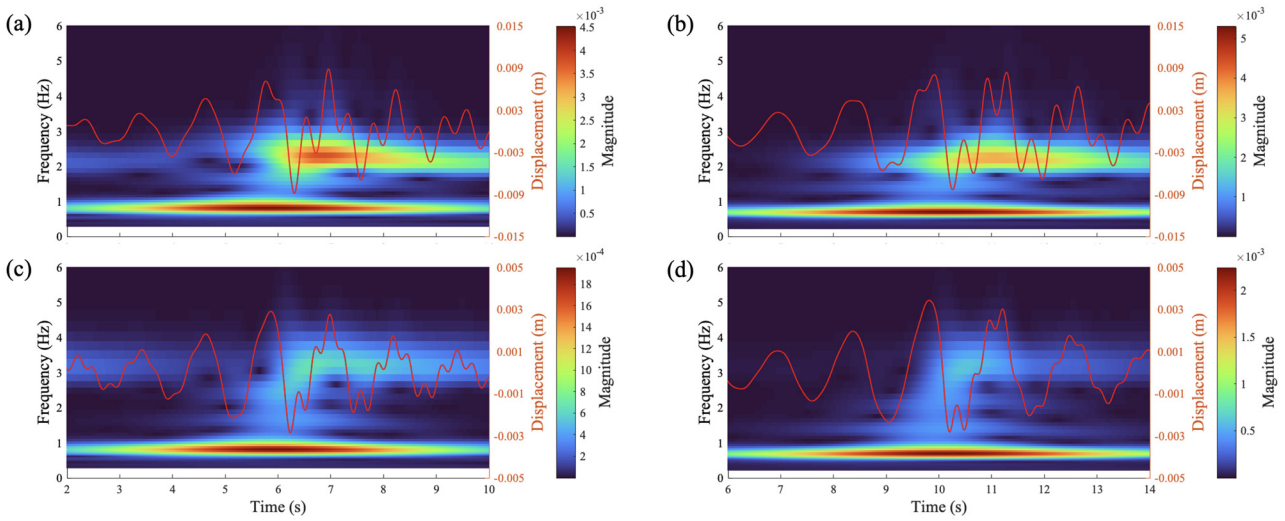

FIG. 13. Contour plots of center point displacement magnitude over frequency and time for a plate with dimensionless plate rigidity β of 72 when relative plate length kL of (a) 1.736 and (b) 1.344, and a plate with β of 180 when kL is of (c) 1.736 and (d) 1.344.

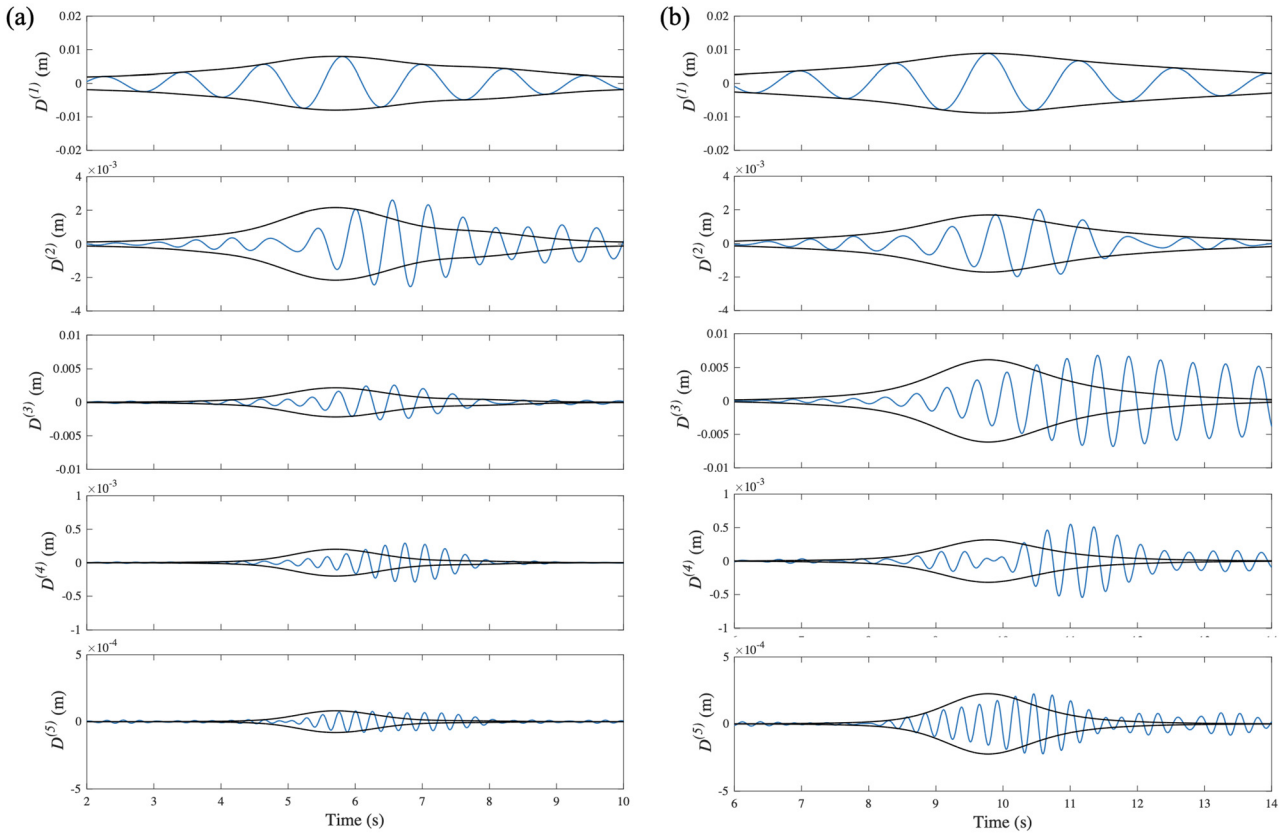

FIG. 14. Time histories of each individual displacement harmonic decomposed by the two-phase method alongside its envelope for a plate with dimensionless plate rigidity β of 54 when relative plate length kL is of (a) 1.736 and (b) 1.344.

06 January 2025 12:39:23

© Author(s) 2025

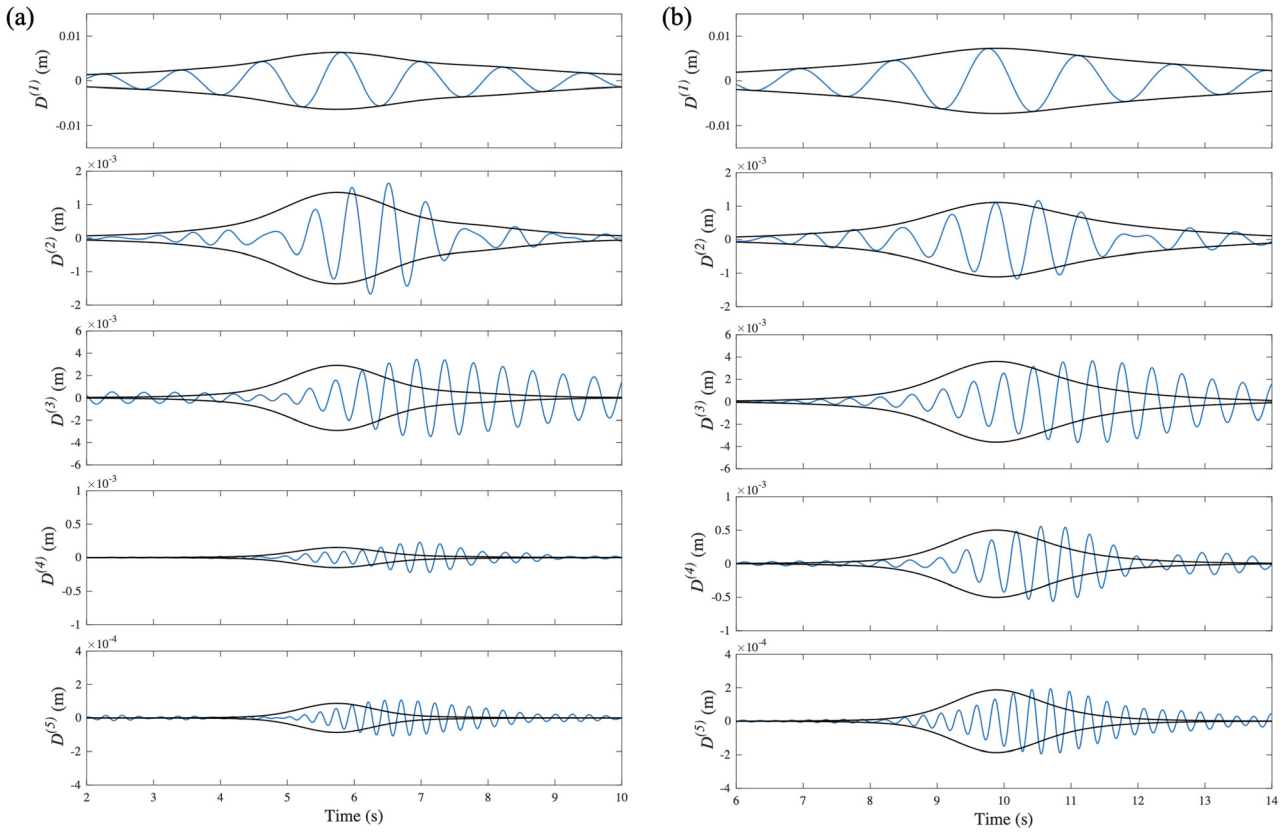

FIG. 15. Time histories of each individual displacement harmonic decomposed by the two-phase method alongside its envelope for a plate with dimensionless plate rigidity β of 72 when relative plate length kL is of (a) 1.736 and (b) 1.344.

resonance occurs at lower-order harmonics, significantly affecting the nonlinear proportions. In this case, the differences in proportions due to varying kL are more pronounced.

When $kL = 1.344$, the third-, fourth-, and fifth-order ratios are larger compared to those at $kL = 1.736$. In contrast, only the second-order ratio is larger for $kL = 1.736$. This phenomenon occurs because larger kL values result in structural resonance at lower-order harmonics. For $kL = 1.736$, structural resonance aligns closely with the second harmonic, leading to a larger second-order ratio. Meanwhile, for $kL = 1.344$, resonance aligns with the third harmonic, resulting in higher third-order ratios and beyond.

In summary, parameters such as plate rigidity and relative plate length significantly influence structural resonance. Structural resonance, in turn, plays a critical role in amplifying nonlinear harmonic proportions, underscoring its importance in the dynamic behavior of submerged plates.

V. CUMULATIVE FATIGUE PERSPECTIVE

Efforts have been made in Refs. 49 and 50 to analyze nonlinear fatigue, but the study focused on rigid structures. As a result, nonlinear fatigue influence was considered only in terms of stress amplitude, overlooking the influence of cycle numbers at various frequencies. There has been a lack of discussion on fatigue analysis for deformable elastic structures, as pointed out in Refs. 51–53. This section will connect the significant nonlinear responses of the plate, discussed previously, to nonlinear stress. It will also demonstrate how the phase-decomposition method potentially contributes to nonlinear fatigue analysis.

A. Relationship between displacement and stress

The phase decomposition method has been proven to cleanly separate each individual point displacement harmonic. This section will confirm the relationship between stress and the center point displacement to highlight the contributions of nonlinear responses to cumulative fatigue relevant to stress.

The approximation of the displacement of the center point of the plate by a quadratic function is a simplification based on the typical behavior of clamped plates under load.[54] Given the boundary conditions for a clamped plate and the assumption of a uniform load or symmetrical loading, the displacement $\omega_p(x_p)$ along the length L of the plate can be approximated near the center using a quadratic function,

$$\omega_p(x_p, t) = \omega_p^{center}(t)\left(1 - \left(\frac{2x_p}{L} - 1\right)^2\right). \tag{19}$$

This approximation satisfies the following conditions: maximum at the center $(\omega_p(x_p = \frac{L}{2}) = \omega_p^{center})$, zero slope at the center

06 January 2025 12:39:23

© Author(s) 2025

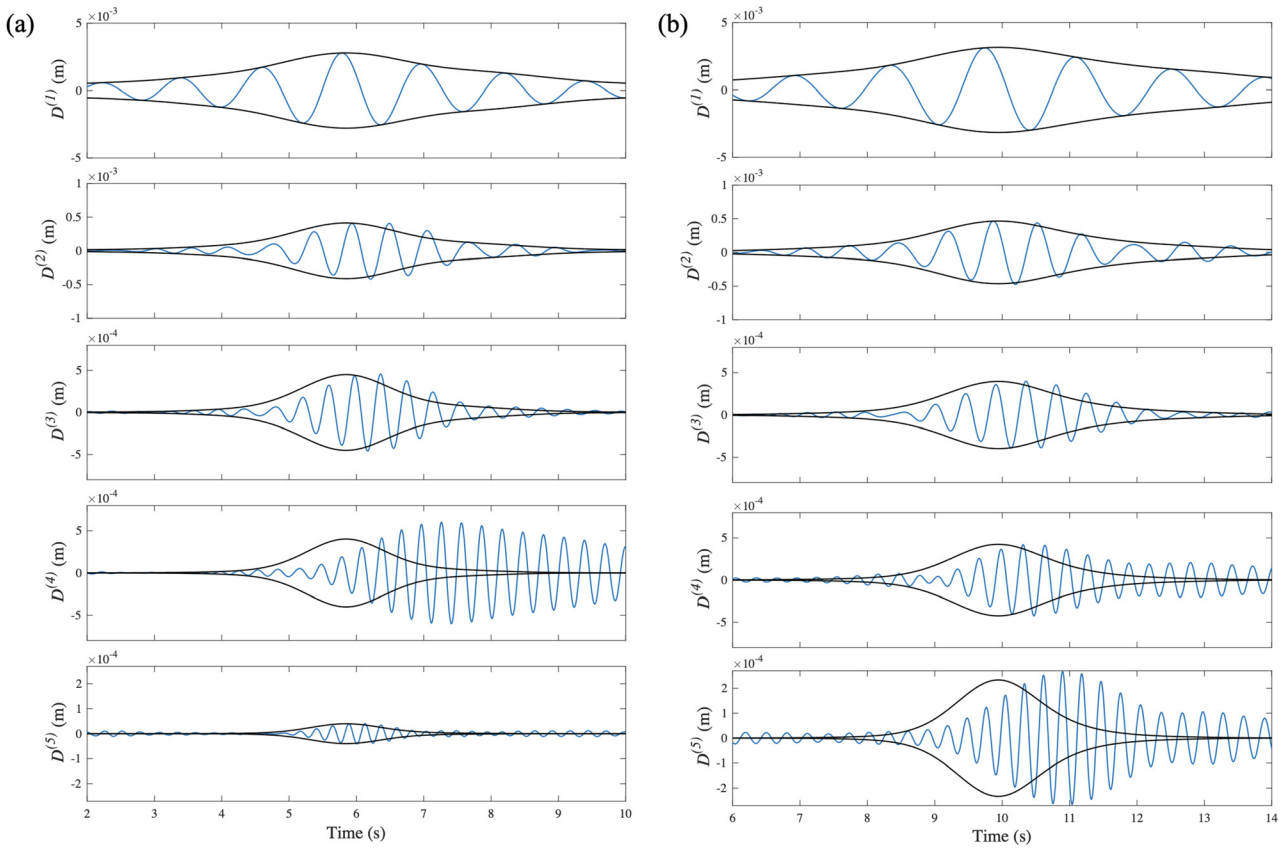

FIG. 16. Time histories of each individual displacement harmonic decomposed by the two-phase method alongside its envelope for a plate with dimensionless plate rigidity β of 180 when relative plate length *kL is* of (a) 1.736 and (b) 1.344.

TABLE II. Proportion of the *nth*-order displacement harmonic to linear component (*nth*-order ratio = *nth*-order harmonic peak value/first-order harmonic peak value) for various plate rigidities and relative plate lengths.

Relative plate length (kL)	1.344					1.736				
Dimensionless plate rigidity (β)	18	36	54	72	180	18	36	54	72	180
Second-order ratio	14.39%	22.61%	22.85%	25.85%	14.72%	25.78%	38.58%	32.75%	26.27%	15.09%
Third-order ratio	18.64%	49.46%	76.63%	52.85%	16.35%	8.52%	16.58%	32.71%	54.51%	16.52%
Fourth-order ratio	1.80%	4.88%	6.05%	3.58%	21.64%	1.16%	2.49%	3.66%	3.58%	21.67%
Fifth-order ratio	1.25%	3.37%	2.53%	1.68%	1.46%	0.37%	0.67%	1.00%	1.69%	1.48%

$(\frac{d\omega_p}{dx_p}|_{x_p=L/2}=0)$, and zero displacement at clamped edges $(\omega_p(0)=\omega_p(L)=0)$, making the approximation reasonable. In this way, the second derivative at the center is

$$\frac{\partial^2\omega_p}{\partial x_p^2}=\omega_p^{center}(t)\left(-\frac{8}{L^2}\right). \tag{20}$$

The bending moment M_x at the center is

$$M_x=-D\frac{\partial^2\omega_p}{\partial x_p^2}=\frac{8D\omega_p^{center}(t)}{L^2}. \tag{21}$$

Here, D is the flexure rigidity of the plate, given by $D=\frac{Eh^3}{12(1-\nu^2)}$, where E denotes Young's modulus, ν refers to Poisson's ratio, and h is the plate thickness. The vertical stress δ_{zz} at the top and bottom surface of the plate is given by

$$\delta_{zz}=\frac{M_x}{I_p}\cdot\pm\frac{L}{2}, \tag{22}$$

where I_p denotes the moment of inertia per unit width, $I_p=\frac{h^3}{12}$. Substituting M_x and I_p and simplifying, we finally obtain

06 January 2025 12:39:23

© Author(s) 2025

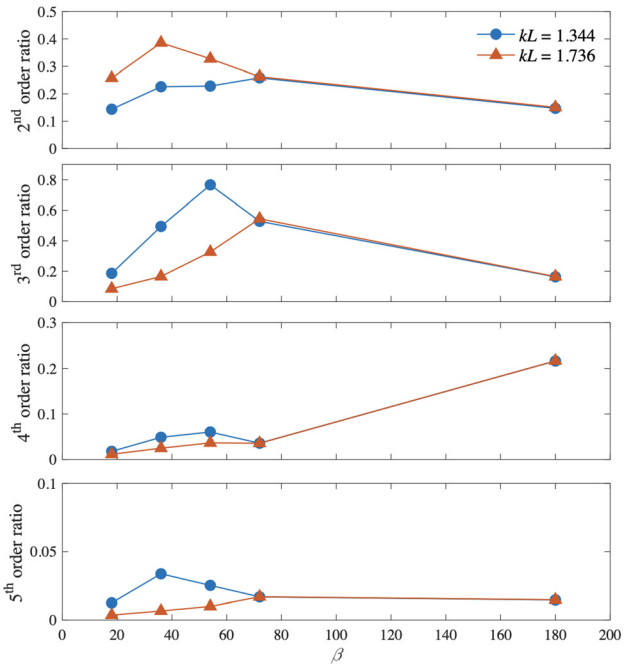

FIG. 17. Proportion of the *nth*-order displacement harmonic to linear component for various plate rigidities and relative plate lengths.

$$\delta_{zz} = \pm \frac{4Eh\omega_p^{center}(t)}{(1-\nu^2)L^2}. \tag{23}$$

In the final formula for δ_{zz}, $\omega_p^{center}(t)$ is the only variable on the right-hand side, indicating that the stress is directly proportional to $\omega_p^{center}(t)$. Using Eq. (23), the vertical stress δ_{zz} for an example case with a dimensionless plate rigidity β of 54 and a relative plate length kL of 1.344 can be derived from the center point displacement. The time histories of the vertical stress for the plate interacting with crest- and trough-focused waves are shown in Fig. 18(a). The two-phase method can be applied here as well, allowing the separation of odd and even harmonics, as illustrated in the amplitude–frequency spectra in Fig. 18(b). By applying the IFFT to each harmonic in the frequency domain, the individual vertical stress harmonics can be obtained as time histories, as shown in Fig. 19, which exhibit the same waveform as the individual center point displacement harmonics in Fig. 10(b).

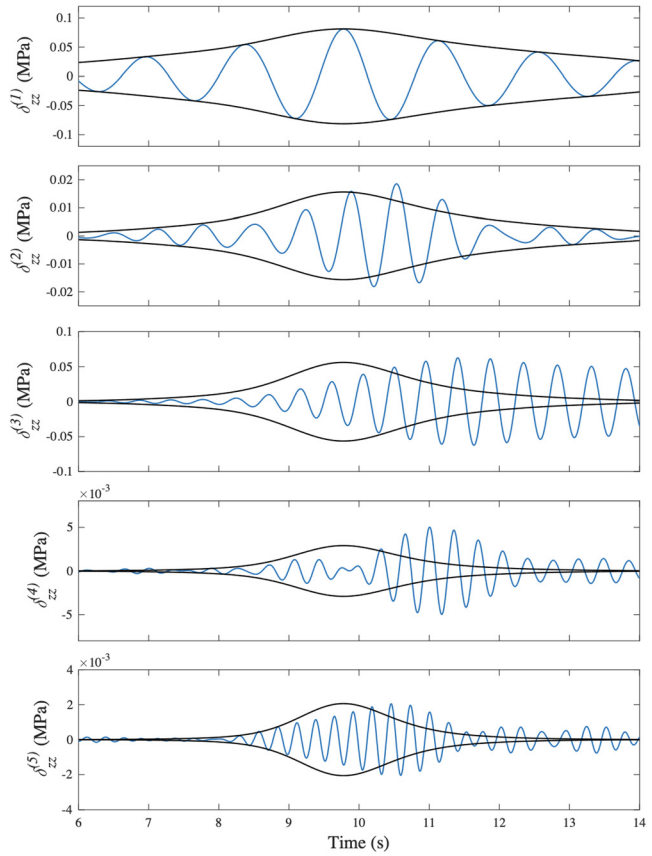

FIG. 19. Time histories of each individual vertical stress harmonic decomposed by the two-phase method alongside its envelope for a plate with a dimensionless plate rigidity β of 54 and a relative plate length kL of 1.344.

By capturing the peak amplitude from the crest of each individual harmonic time–stress curve, the ratio of the *nth*-order vertical stress harmonic to the linear vertical stress can be determined. This ratio mirrors that of the center point displacement harmonics, with the third harmonic reaching the largest nonlinear proportion, at 76.63% of the linear component, due to structural resonance. The proportion of each individual vertical stress harmonic corresponds to the same value in Table II for the corresponding harmonics, as indicated by Eq. (23).

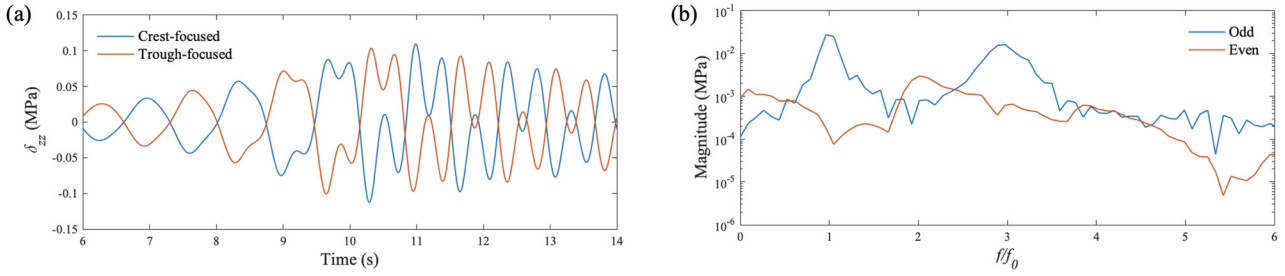

FIG. 18. (a) Crest- and trough-focused vertical stress in time histories and (b) vertical stress magnitude spectra of separated harmonic groups by the two-phase method for a plate with a dimensionless plate rigidity β of 54 and a relative plate length kL of 1.344.

06 January 2025 12:39:23

© Author(s) 2025

Thus, the direct proportionality between stress and center point displacement demonstrates that nonlinear responses significantly contribute to fatigue. The clean separation of these stress-related responses provides a novel and effective approach to cumulative fatigue calculations.

B. Fatigue assessment methods

In fatigue analysis for design, resistance to fatigue damage is represented by an SN curve. The simplest, conservative form of this curve is expressed as[49]

$$N = as^{-m}, \tag{24}$$

where N is the number of cycles to failure at a constant stress range s, and a and m are parameters of the SN curve. Fatigue damage, D, accumulated over a period can be calculated using the Palmgren–Miner linear cumulative damage rule

$$D = \frac{1}{a}\sum_{i=1}^{n} s_i^m, \tag{25}$$

where s_i is the range of the *ith* stress cycle, and n is the total number of cycles during the certain period.

To calculate the accumulated fatigue damage, the spectral fatigue damage assessment method assumes that wave-induced stress variations in specific sea states are a narrow-band Gaussian process, and the peak values of the stress follow a Rayleigh distribution. Based on these assumptions, the stress response spectral density function is obtained, which is then used to calculate the cumulative fatigue damage in a given sea state.

However, the assumptions of the spectral method are not sufficiently accurate, especially for the elastic plate with significant nonlinear responses induced by structural resonance, as highlighted in Sec. IV, which has been shown to be directly proportional to stress in Sec. IV A. In contrast to the spectral method, the time-domain analysis method can assess structural fatigue damage through coupled dynamic analysis and the rainflow counting method. This method uses a time history of wave kinematics generated from a specific wave spectrum, applying hydrodynamic loads to the structural model while accounting for nonlinear effects. Once the stress history is obtained, the rainflow counting method is used to count the number of cycles corresponding to each stress range. With the known occurrence probability of a specific sea state, the fatigue damage caused by that sea state can be calculated using the Palmgren–Miner Rule. However, time-domain analysis has disadvantages, including a complicated calculation procedure and extensive computational time.

This study demonstrates that stress derived from the center point displacement can be decomposed into a fundamental harmonic that closely aligns with the spectral peak frequency of the incident waves, alongside higher-order harmonics that occur at integer multiples of the fundamental frequency. These higher harmonics result from nonlinearities in wave–structure interactions and structural resonance. By employing the phase-decomposition method, each individual harmonic of displacement is cleanly separated, enabling accurate stress calculations for each frequency. These stresses, considered deterministic periodic values, facilitate the estimation of total occurrences and separated damages at each frequency over a given time duration,

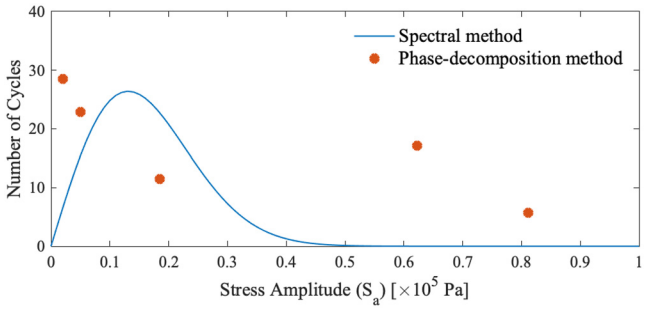

FIG. 20. Comparison of stress cycle numbers estimated using the spectral method and the phase-decomposition method.

providing a more realistic prediction of cumulative fatigue damage under specific sea states.

Figure 20 compares the stress cycle numbers estimated by the traditional spectral method and the phase-decomposition method for the example case in Sec. IV A. The traditional spectral method, based on Rayleigh distribution,[55] predicts the probability density of stress amplitudes S_a as follows:

$$p(S_a) = \frac{S_a}{M_0}\exp\left(-\frac{S_a^2}{2M_0}\right), \tag{26}$$

where M_0 is the zeroth moment of the power spectral density, calculated as

$$M_0 = \int_0^\infty S(f)df. \tag{27}$$

In this research, the power spectral density is based on the JONSWAP spectrum used in OpenFOAM,

$$S(f) = \alpha H_s^2 f_0^4 f^{-5}\gamma^\beta \exp\left(-\frac{5}{4}\left(\frac{f_0}{f}\right)^4\right), \tag{28}$$

where f_0 is the peak frequency of the incident wave group, the scaling parameter, $\alpha = \frac{0.0624}{0.230+0.0336\gamma-\frac{0.185}{1.9+\gamma}}$, the shape parameter, $\beta = \exp\left(-\frac{(f-f_0)^2}{2\sigma^2 f_0^2}\right)$, the spectral width, $\sigma = 0.07$ when $f < f_0$ and $\sigma = 0.09$ when $f \geq f_0$, and the enhancement factor, $\gamma = 3.3$. Using this spectrum, the number of stress cycles during a total exposure time T_{total} is given by

$$N(S_a) = p(S_a)\cdot T_{total}\cdot f_0. \tag{29}$$

In contrast, the phase-decomposition method derives individual stress harmonics at specific frequencies, as shown in Fig. 19. Using the peak value of each harmonic as the deterministic stress amplitude, the number of stress cycles for the *nth* harmonic is calculated as

$$N = T_{total}\cdot nf_0. \tag{30}$$

This study considers harmonics up to the fifth order, though the phase-decomposition method can extend to higher orders, as shown in Ref. 56. Figure 20 illustrates the stress cycle numbers for the first to fifth-order harmonics, showing general agreement with the stress amplitude range predicted by the spectral method. However, the spectral method predicts stress based solely on wave characteristics,

06 January 2025 12:39:23

© Author(s) 2025

ignoring complex wave–structure interactions and structural resonance. In contrast, the results separated by the phase-decomposition method are directly simulated by the fully nonlinear CFD+CSM model, demonstrating that stress cycles are scattered rather than constant spectral values.

The phase-decomposition method enables efficient and realistic calculations of stress cycles at specific frequencies, considering wave–structure interactions and resonance. Furthermore, Fig. 20 emphasizes the significant contribution of third-order harmonics in structural fatigue, which exhibit substantial stress amplitudes and tripled cycle numbers compared to the linear component. This underscores the necessity of fully nonlinear models for accurately evaluating the responses of elastic structures.

In this research, irregular waves in a focused wave format are investigated. This method can also be applied to random irregular waves over the long term[57] and to different wave spreading conditions,[58] which are considered similarly applicable for long-term and real-sea-state responses. In this way, cumulative fatigue calculations can widely utilize this method for a certain sea state.

VI. CONCLUSIONS

This paper employs the CFD+CSM model to investigate the nonlinear hydroelastic responses of a submerged horizontal plate under focused wave conditions, which is a topic not previously addressed in the literature. The phase-decomposition method is successfully utilized to cleanly separate the individual harmonics of the nonlinear displacement at the center point of the plate. By demonstrating that stress is directly proportional to the center point displacement, a cumulative fatigue damage analysis is discussed. The following key findings are derived from this study:

- The interaction of focused waves with submerged horizontal plates of varying plate rigidities reveals that higher-order harmonics are significantly influenced by structural resonance. The proportion of these harmonics changes with increasing rigidity, initially increasing and then decreasing for larger β value. The clean separation of individual harmonics highlights the complex interplay between wave-induced displacements and structural properties.
- The time–frequency contour plots and time–displacement curves illustrate how different plate rigidities influence the interaction of focused waves with submerged horizontal plates. Higher-order harmonics are significantly affected by structural resonance, with the extent of this influence varying based on plate rigidity and relative length. As plate rigidity increases, the prominence of higher-order harmonics shifts, with resonance effects more pronounced at specific frequencies.
- Traditional fatigue assessment methods, such as the spectral and time-domain analysis methods, have limitations. The spectral method assumes narrow-band Gaussian processes and Rayleigh-distributed stress peaks, which is inadequate for elastic plates with significant nonlinear responses from structural resonance. The time-domain method, while accurate, is complex and computationally intensive. This research uses a phase-decomposition method that cleanly separates each displacement harmonic and accurately derives stress at specific frequencies. By treating these stresses as deterministic periodic values, this approach potentially allows for the quick and accurate determination of stress ranges and cycle counts in various sea states, improving cumulative fatigue damage assessments for marine industries.

While this study provides valuable insights into the nonlinear responses and fatigue assessments of submerged horizontal plates, limitations should be noted. This research aims to investigate the interactions under focused wave conditions, and long-term random waves are not considered in this study. While new methods have been proposed using the phase-decomposition method, no practical long-term wave regime case studies have been discussed at this stage. Additionally, the assumption of linear material properties (represented by dimensionless plate rigidity β) for the plate may not fully capture the behavior of more complex, nonlinear materials used in real-world applications. Future work should focus on extending the methodology to account for these factors, as well as validating the findings against experimental data.

ACKNOWLEDGMENTS

The authors are very grateful for the financial support from the UK EPSRC [Grant Nos. EP/T026782/1; EP/V050079/1; and EP/V040235/1].

AUTHOR DECLARATIONS

Conflict of Interest

The authors have no conflicts to disclose.

Author Contributions

Haoyu Ding: Conceptualization (equal); Formal analysis (lead); Investigation (equal); Methodology (equal); Software (equal); Validation (equal); Visualization (lead); Writing – original draft (lead). **Luofeng Huang:** Conceptualization (equal); Investigation (equal); Methodology (equal); Software (equal); Validation (equal); Writing – review & editing (equal). **Jun Zang:** Conceptualization (equal); Funding acquisition (lead); Resources (lead); Supervision (lead); Writing – review & editing (equal).

DATA AVAILABILITY

The data that support the findings of this study are available from the corresponding author upon reasonable request.

REFERENCES

[1]A. G. Greenhill, "Wave motion in hydrodynamics," Am. J. Math. **9**, 62–96 (1886).
[2]D. V. Evans and T. V. Davies, "Wave-ice interaction," Technical Report No. 1313, 1968.
[3]C. Fox and V. A. Squire, "On the oblique reflexion and transmission of ocean waves at shore fast sea ice," Philos. Trans. R. Soc. London, Ser. A **347**, 185–218 (1994).
[4]C. Fox and V. A. Squire, "Reflection and transmission characteristics at the edge of shore fast sea ice," J. Geophys. Res.: Oceans **95**, 11629–11639, https://doi.org/10.1029/JC095iC07p11629 (1990).
[5]V. A. Squire, J. P. Dugan, P. Wadhams, P. J. Rottier, and A. K. Liu, "Of ocean waves and sea ice," Annu. Rev. Fluid Mech. **27**, 115–168 (1995).
[6]A. E. Heins, "Water waves over a channel of finite depth with a submerged plane barrier," Can. J. Math. **2**, 210–222 (1950).
[7]T. R. Greene and A. E. Heins, "Water waves over a channel of infinite depth," Q. Appl. Math. **11**, 201–214 (1953).

06 January 2025 12:39:23

© Author(s) 2025

[8]J. E. Burke, "Scattering of surface waves on an infinitely deep fluid," J. Math. Phys. **5**, 805–819 (1964).
[9]M. Patarapanich, "Maximum and zero reflection from submerged plate," J. Waterw. Port Coastal Ocean Eng. **110**, 171–181 (1984).
[10]P. F. Siew and D. G. Hurley, "Long surface waves incident on a submerged horizontal plate," J. Fluid Mech. **83**, 141–151 (1977).
[11]T. Ijima, S. Ozaki, Y. Eguchi, and A. Kobayashi, "Breakwater and quay well by horizontal plates," Coastal Eng. **1970**, 1537–1556.
[12]P. L. Liu and M. Iskandarani, "Scattering of short-wave groups by submerged horizontal plate," J. Waterw. Port Coastal Ocean Eng. **117**, 235–246 (1991).
[13]K. H. Wang and Q. Shen, "Wave motion over a group of submerged horizontal plates," Int. J. Eng. Sci. **37**, 703–715 (1999).
[14]M. U. Hassan, M. H. Meylan, and M. A. Peter, "Water-wave scattering by submerged elastic plates," Q. J. Mech. Appl. Math. **62**, 321–344 (2009).
[15]S. C. Mohapatra and T. Sahoo, "Wave interaction with a floating and submerged elastic plate system," J. Eng. Math. **87**, 47–71 (2014).
[16]R. Porter, "Linearised water wave problems involving submerged horizontal plates," Appl. Ocean Res. **50**, 91–109 (2015).
[17]P. Qi and Y. J. Hou, "Numerical wave flume study on wave motion around submerged plates," China Ocean Eng. **17**, 397–406 (2003).
[18]H. Jin, Y. Liu, S. He, and H. Li, "Numerical study on the wave dissipating performance of a submerged horizontal plate breakwater using OpenFOAM," in Proceedings of the Eleventh ISOPE Pacific/Asia Offshore Mechanics Symposium, Shanghai, China, October 2014, Paper No. ISOPE-P-14-065.
[19]M. He, W. Xu, X. Gao, and B. Ren, "The layout of submerged horizontal plate breakwater (SHPB) with respect to the tidal-level variation," Coastal Eng. J. **60**, 280–298 (2018a).
[20]M. He, X. Gao, W. Xu, B. Ren, and H. Wang, "Potential application of submerged horizontal plate as a wave energy breakwater: A 2D study using the WCSPH method," Ocean Eng. **185**, 27–46 (2019).
[21]M. He, W. Xu, X. Gao, and B. Ren, "SPH simulation of wave scattering by a heaving submerged horizontal plate," Int. J. Ocean Coastal Eng. **01**, 1840004 (2018b).
[22]D. Fu, X. Zhao, S. Wang, and D. Yan, "Numerical study on the wave dissipating performance of a submerged heaving plate breakwater," Ocean Eng. **219**, 108310 (2021).
[23]C. Yueh, S. Chuang, and C. Wen, "Bragg reflection of water waves due to submerged wavy plate breakwater," J. Hydro-environ. Res. **21**, 52–59 (2018).
[24]L. Huang, "An opensource solver for wave-induced FSI problems," in Proceedings of CFD with OpenSource Software, 2018.
[25]L. Huang, K. Ren, M. Li, Ž. Tuković, P. Cardiff, and G. Thomas, "Fluid-structure interaction of a large ice sheet in waves," Ocean Eng. **182**, 102–111 (2019).
[26]L. Huang and Y. Li, "Design of the submerged horizontal plate breakwater using a fully coupled hydroelastic approach," Comput.-Aided Civ. Infrastruct. Eng. **37**, 915–932 (2022).
[27]Ž. Tuković, A. Karač, P. Cardiff, H. Jasak, and A. Ivanković, "OpenFOAM finite volume solver for fluid-solid interaction," Trans. FAMENA **42**, 1–31 (2018).
[28]P. Cardiff, A. Karač, P. De Jaeger, H. Jasak, J. Nagy, A. Ivanković, and Ž. Tuković, "An open-source finite volume toolbox for solid mechanics and fluid-solid interaction simulations," arXiv:1808.10736 [math.NA] (2018).
[29]L. Huang, Y. Li, D. Benites-Munoz, C. W. Windt, A. Feichtner, S. Tavakoli, J. Davidson, R. Paredes, T. Quintuna, E. Ransley *et al.*, "A review on the modelling of wave-structure interactions based on OpenFOAM," OpenFOAM J. **2**, 116–142 (2022).
[30]P. H. Wirsching, T. L. Paez, and K. Ortiz, *Random Vibrations: Theory and Practice* (Courier Corporation, 2006).
[31]M. Matsuishi and T. Endo, *Fatigue of Metals Subjected to Varying Stress* (Japan Society of Mechanical Engineers, Fukuoka, Japan, 1968), Vol. 68, pp. 37–40.
[32]R. I, "A new definition of the rainflow cycle counting method," Int. J. Fatigue **9**, 119–121 (1987).
[33]Z. Gao and T. Moan, "Frequency-domain fatigue analysis of wide-band stationary Gaussian processes using a trimodal spectral formulation," Int. J. Fatigue **30**, 1944–1955 (2008).
[34]Y. Low, "Extending a time/frequency domain hybrid method for riser fatigue analysis," Appl. Ocean Res. **33**, 79–87 (2011).
[35]S. O. Rice, "Mathematical analysis of random noise," Bell Syst. Tech. J. **23**, 282–332 (1944).
[36]P. H. Wirsching and M. C. Light, "Fatigue under wide band random stresses," J. Struct. Div. **106**, 1593–1607 (1980).
[37]D. Benasciutti and R. Tovo, "Spectral methods for lifetime prediction under wide-band stationary random processes," Int. J. Fatigue **27**, 867–877 (2005).
[38]C. Braccesi, F. Cianetti, G. Lori, and D. Pioli, "Fatigue behaviour analysis of mechanical components subject to random bimodal stress process: Frequency domain approach," Int. J. Fatigue **27**, 335–345 (2005).
[39]ABS, *Guide for the Fatigue Assessment of Offshore Structures* (American Bureau of Shipping, 2003).
[40]J. Zang, P. H. Taylor, G. Morgan, M. Tello, J. Grice, and J. Orszaghova, "Experimental study of non-linear wave impact on offshore wind turbine foundations," in Proceedings of the 3rd International Conference on the Application of Physical Modelling to Port and Coastal Protection (Coastlab2010), Barcelona, Spain, 2010.
[41]N. G. Jacobsen, D. R. Fuhrman, and J. Fredsøe, "A wave generation toolbox for the open-source CFD library: OpenFOAM®," Int. J. Numer. Methods Fluids **70**, 1073–1088 (2012).
[42]H. Ding, Q. Chen, and J. Zang, "Numerical simulation of wave interactions with floating offshore renewable energy structures: A comparative study between a particle-based pic model and OpenFOAM," J. Fluids Struct. **126**, 104092 (2024).
[43]J. Gao, C. Mi, Z. Song, and Y. Liu, "Transient gap resonance between two closely-spaced boxes triggered by nonlinear focused wave groups," Ocean Eng. **305**, 117938 (2024).
[44]J. Gao, X. Ma, J. Zang, G. Dong, X. Ma, Y. Zhu, and L. Zhou, "Numerical investigation of harbor oscillations induced by focused transient wave groups," Coastal Eng. **158**, 103670 (2020).
[45]M. Christou and K. Ewans, "Field measurements of rogue water waves," J. Phys. Oceanogr. **44**, 2317–2335 (2014).
[46]D. K. K. Sree, A. W. Law, and H. H. Shen, "An experimental study on the interactions between surface waves and floating viscoelastic covers," Wave Motion **70**, 195–208 (2017).
[47]G. G. Stokes, *On the Theory of Oscillatory Waves* (Pitt Press, 1847), Vol. 8, pp. 441–455.
[48]L. F. Chen, J. Zang, P. H. Taylor, L. Sun, G. C. Morgan, J. Grice, J. Orszaghova, and M. Tello Ruiz, "An experimental decomposition of nonlinear forces on a surface-piercing column: Stokes-type expansions of the force harmonics," J. Fluid Mech. **848**, 42–77 (2018).
[49]I. Drummen, M. Wu, M. L. Kaminski, and T. Moan, "Numerical investigation into the application of response conditioned waves for long-term nonlinear fatigue analyses of rigid hulls," Ocean Eng. **36**, 1208–1216 (2009).
[50]A. Marjan and L. Huang, "Topology optimisation of offshore wind turbine jacket foundation for fatigue life and mass reduction," Ocean Eng. **289**, 116228 (2023).
[51]Z. Hu, L. Huang, and Y. Li, "Fully-coupled hydroelastic modeling of a deformable wall in waves," Coastal Eng. **179**, 104245 (2023).
[52]C. Luo and L. Huang, "Energy efficiency analysis of a deformable wave energy converter using fully coupled dynamic simulations," Oceans **5**, 227–243 (2024).
[53]Y. Wei, C. Wang, W. Chen, and L. Huang, "Array analysis on a seawall type of deformable wave energy converters," Renewable Energy **225**, 120344 (2024).
[54]H. Takabatake, *Simplified Analytical Methods of Elastic Plates*, 1st ed. (Springer, Singapore, 2018).
[55]S.-D. Wu, D.-G. Shang, P.-C. Liu, G.-C. Hao, G. Hou, F.-T. Shi, and B. Miao, "Fatigue life prediction based on modified narrowband method under broadband random vibration loading," Int. J. Fatigue **159**, 106832 (2022).
[56]X. Feng, P. Taylor, S. Dai, A. Day, R. Willden, and T. Adcock, "Experimental investigation of higher harmonic wave loads and moments on a vertical cylinder by a phase-manipulation method," Coastal Eng. **160**, 103747 (2020).
[57]T. A. A. Adcock, X. Feng, T. Tang, B. van den, S. Ton, S. Day, S. Dai, Y. Li, Z. Lin, W. Xu, and P. H. Taylor, "Application of phase decomposition to the analysis of random time series from wave basin tests," in Proceedings of the ASME 2019 38th International Conference on Ocean, Offshore and Arctic Engineering, 2019, Paper No. V009T12A020.
[58]H. Ding, G. Zhao, T. Tang, P. H. Taylor, T. A. A. Adcock, S. Dai, D. Ning, L. Chen, J. Li, R. Wang, and J. Zang, "Experimental investigation of nonlinear forces on a monopile offshore wind turbine foundation under directionally spread waves," J. Offshore Mech. Arct. Eng. **147**, 042002 (2025).

06 January 2025 12:39:23

© Author(s) 2025

https://dspace.org/

Nonlinear hydroelastic responses of a submerged horizontal plate under focused wave conditions: a cumulative fatigue perspective

Ding, Haoyu; Huang, Luofeng; Zang, Jun

2025-01-31
American Institute of Physics (AIP)
https://doi.org/10.1063/5.0246534
Ding H, Huang L, Zang J. (2025) Nonlinear hydroelastic responses of a submerged horizontal plate under focused wave conditions: a cumulative fatigue perspective. Physics of Fluids, Volume 37, Issue 1, January 2025, Article number 017110

Downloaded from a DSpace repository. https://dspace.org/